




# CO and [C II] line emission of molecular clouds: the impact of stellar feedback and non-equilibrium chemistry

S. Ebagezio <sup>1</sup>\*, D. Seifried <sup>1,2</sup>, S. Walch<sup>1,2</sup>, P. C. Nürnbergger<sup>1</sup>, T.-E. Rathjen <sup>1</sup> and T. Naab<sup>3</sup>

<sup>1</sup>Universität zu Köln, I. Physikalisches Institut, Zùlpicher Str. 77, D-50937 Köln, Germany

<sup>2</sup>Center for Data and Simulation Science, University of Cologne, Albertus-Magnus-Platz, D-50923 Köln, Germany

<sup>3</sup>Max Planck Institute for Astrophysics, Karl-Schwarzschild-Str. 1, D-85748 Garching, Germany

Accepted 2023 August 25. Received 2023 July 28; in original form 2022 July 11

## ABSTRACT

We analyse synthetic  $^{12}\text{CO}$ ,  $^{13}\text{CO}$ , and [C II] emission maps of molecular cloud (MC) simulations from the SILCC-Zoom project. We present radiation, magnetohydrodynamic zoom-in simulations of individual clouds, both with and without radiative stellar feedback, forming in a turbulent multiphase interstellar medium following on-the-fly the evolution of e.g.  $\text{H}_2$ , CO, and  $\text{C}^+$ . We introduce a novel post-processing routine based on CLOUDY which accounts for higher ionization states of carbon due to stellar radiation in H II regions. Synthetic emission maps of [C II] in and around feedback bubbles show that the bubbles are largely devoid of [C II], as recently found in observations, which we attribute to the further ionization of  $\text{C}^+$  into  $\text{C}^{2+}$ . For both  $^{12}\text{CO}$  and  $^{13}\text{CO}$ , the cloud-averaged luminosity ratio,  $L_{\text{CO}}/L_{[\text{C II}]}$ , can neither be used as a reliable measure of the  $\text{H}_2$  mass fraction nor of the evolutionary stage of the clouds. We note a relation between the  $I_{\text{CO}}/I_{[\text{C II}]}$  intensity ratio and the  $\text{H}_2$  mass fraction for individual pixels of our synthetic maps. The scatter, however, is too large to reliably infer the  $\text{H}_2$  mass fraction. Finally, the assumption of chemical equilibrium overestimates  $\text{H}_2$  and CO masses by up to 150 and 50 per cent, respectively, and  $L_{\text{CO}}$  by up to 60 per cent. The masses of H and  $\text{C}^+$  would be underestimated by 65 and 30 per cent, respectively, and  $L_{[\text{C II}]}$  by up to 35 per cent. Hence, the assumption of chemical equilibrium in MC simulations introduces intrinsic errors of a factor of 2 in chemical abundances, luminosities, and luminosity ratios.

**Key words:** astrochemistry – radiative transfer – methods: numerical – ISM: clouds – H II regions – ISM: molecules.

## 1 INTRODUCTION

Molecular clouds (MCs) are defined as those regions of the interstellar medium (ISM) where hydrogen exists predominantly in its molecular form,  $\text{H}_2$ . Due to the absence of dipole moment and low temperatures, typically of a few 10 K,  $\text{H}_2$  is not directly observable in MCs. Nevertheless, information on the abundance and distribution of  $\text{H}_2$  are of great importance because they allow us to identify the star formation sites in MCs.  $\text{H}_2$  is observed only indirectly by means of dust continuum (see e.g. Bot et al. 2007) and molecules which trace its presence. The most used molecule to trace  $\text{H}_2$  in MCs is CO (e.g. Wilson, Jefferts & Penzias 1970; Scoville & Solomon 1975; Larson 1981; Solomon et al. 1987; Dame, Hartmann & Thaddeus 2001; Bolatto, Wolfire & Leroy 2013; Dobbs et al. 2014). In order to infer the amount of  $\text{H}_2$  from the observations of CO, a conversion factor  $X_{\text{CO}}$  from the observed CO luminosity into a  $\text{H}_2$  column density has been established (see e.g. Scoville et al. 1987; Dame et al. 1993; Strong & Mattox 1996; Melchior et al. 2000; Lombardi et al. 2006; Nielen et al. 2006; Smith et al. 2012; Bolatto et al. 2013; Ripple et al. 2013). The standard value of  $X_{\text{CO}}$  in the Milky Way is commonly assumed to be  $X_{\text{CO}} = 2 \times 10^{20} \text{ cm}^{-2} \text{ K}^{-1} \text{ km}^{-1} \text{ s}$ , but there is plenty of evidence that the actual value strongly depends on the environmental conditions (Glover & Mac Low 2011; Shetty et al.

2011a; Bolatto et al. 2013; Gong et al. 2020; Seifried et al. 2020a) or the cloud's evolutionary stage (Borchert et al. 2022). Furthermore, because of this strong dependence, it is used to assess the total amount of  $\text{H}_2$  in a cloud, but it cannot be easily used on sub-pc scales (e.g. Bisbas, Tan & Tanaka 2021). More in general, CO is not a perfect tracer for  $\text{H}_2$  because of (i) the presence of CO-dark areas, which may contain a significant amount of  $\text{H}_2$ , but almost no CO (see for instance Lada & Blitz 1988; van Dishoeck & Black 1988; Grenier, Casandjian & Terrier 2005; Glover & Mac Low 2011; Glover & Clark 2016; Seifried et al. 2020a), and (ii) the optical thickness of CO in denser regions, which break the quantitative relation between the CO luminosity and the  $\text{H}_2$  mass (e.g. Seifried et al. 2020a; Bisbas et al. 2021).

Other chemical species are also used to assess the  $\text{H}_2$  abundance in the clouds: neutral carbon emission has been studied in this context and an  $X_{\text{C}}$ -factor (Papadopoulos, Thi & Viti 2004; Offner et al. 2014), defined in an analogous way than  $X_{\text{CO}}$ , has been used to assess the abundance of  $\text{H}_2$  in MCs. The value of  $X_{\text{C}}$ , however, also depends on the clouds' environment (Offner et al. 2014; Bisbas et al. 2021).  $\text{C}^+$  is another frequently abundant form of carbon, which has been studied intensively in MCs and is one of the main coolants of the ISM (Tielens & Hollenbach 1985; Stacey et al. 1991; Stutzki 2001; Röllig et al. 2006; Appleton et al. 2013; Lesaffre et al. 2013; Ossenkopf et al. 2013; Pineda et al. 2013; Beuther et al. 2014; Pineda, Langer & Goldsmith 2014; Klessen & Glover 2016, and many more). It is most abundant in photo-dissociation regions (Ossenkopf et al. 2013) and

\* E-mail: [ebagezio@ph1.uni-koeln.de](mailto:ebagezio@ph1.uni-koeln.de)

in shock fronts (Appleton et al. 2013; Lesaffre et al. 2013). Some studies (e.g. Velusamy & Langer 2014; Franeck et al. 2018) suggest that  $C^+$  is a tracer of some CO-dark areas of the clouds. However, a reliable relation between the  $C^+$  emission and the  $H_2$  abundance is difficult to establish, because most of the [C II] emission comes from regions which are predominantly atomic (Franeck et al. 2018).

The formation and evolution of MCs has been studied with numerical simulations in a large number of recent works (e.g. Dobbs & Pringle 2013; Smith et al. 2014a; Gatto et al. 2015; Li et al. 2015; Walch et al. 2015; Ibáñez-Mejía et al. 2016; Padoan et al. 2016; Seifried et al. 2017; Kim & Ostriker 2018, and many more). Chemistry treatment is generally performed in two possible ways: one option is to first run the simulations without considering the chemical composition of the clouds and then post-process the chemistry assuming equilibrium (e.g. Gong, Ostriker & Kim 2018; Li et al. 2018; Gong et al. 2020; Keating et al. 2020). Post-processing the chemistry enables the use of complex networks, but the assumption of chemical equilibrium is necessary and, as a consequence, the H abundance is usually underestimated while  $H_2$  is overestimated (Hu, Sternberg & van Dishoeck 2021; Borchert et al. 2022; Seifried et al. 2022). Conversely, some other simulations include a treatment of molecule formation with a non-equilibrium chemical network (Clark et al. 2012; Smith et al. , 2020; Smith, Glover & Klessen 2014c; Walch et al. 2015; Hu et al. 2016, 2017, 2021; Seifried & Walch 2016; Valdivia et al. 2016; Lahén et al. 2020; Rathjen et al. 2021). This usually implies the usage of simpler networks but the assumption of chemical equilibrium is avoided. Recently, non-equilibrium chemistry has been joined with high-resolution simulations. For instance, in the SILCC-Zoom project (Seifried et al. 2017, 2020a; Haid et al. 2019), the formation of MCs is followed from spatial scales of several hundred parsec down to  $\sim 0.1$  pc. These simulations serve as a basis of this publication.

In this paper, we produce synthetic observations of these simulated MCs using the RADMC-3D radiative transfer code (Dullemond et al. 2012) in order to investigate (i) the usability of the CO/[C II] emission line ratio as an alternative tracer (to  $X_{CO}$ ) for the prevailing  $H_2$  gas mass, and (ii) its potential of being used as an indicator of MC evolution. We also shed light on the role of the assumption of equilibrium chemistry on the emission of CO and [C II].

This paper is structured as follows: in Sections 2 and 3, we describe the numerical methods which we use to run the simulations and the radiative transfer calculations. In Section 4 we describe the overall aspect of the simulations, the corresponding synthetic observations, the  $X_{CO}$  factor, and the line ratios, considering both the total luminosity and the intensity from single pixels. Then, we discuss our results and we analyse the importance of the equilibrium chemistry in Section 5. Finally, we summarize our results in Section 6.

## 2 SILCC-ZOOM SIMULATIONS

The simulated MCs we use in this paper are part of the SILCC-Zoom project (Seifried et al. 2017). The zoom-in simulations are performed within the SILCC project (see Walch et al. 2015; Girichidis et al. 2016, 2018; Gatto et al. 2017; Peters et al. 2017; Rathjen et al. 2021, 2023 for details).

The SILCC setup models a region of a stratified galactic disc. The rectangular box measures  $500 \text{ pc} \times 500 \text{ pc} \times \pm 5 \text{ kpc}$ , and uses periodic boundary conditions in  $x$ - and  $y$ -direction, while outflow boundary conditions are applied in the  $z$ -direction. The simulations are performed with the adaptive mesh refinement (AMR) code FLASH 4.3 (Fryxell et al. 2000; Dubey, Reid & Fisher 2008) and use, for the hydrodynamics (HD) runs, a solver described in Bouchut,

Klingenberg & Waagan (2007) and Waagan (2009), which guarantees positive entropy and density. The magnetohydrodynamical (MHD) runs use an entropy-stable solver (Derigs et al. 2016, 2018). We model the chemical evolution of the ISM using a chemical network for  $H^+$ , H,  $H_2$ ,  $C^+$ , O, CO, and  $e^-$  (Nelson & Langer 1997, hereafter NL97; Glover & Mac Low 2007a, b; Glover et al. 2010), which also follows the thermal evolution of the gas including the most important heating and cooling processes. We assume solar metallicity with elemental abundances of carbon and oxygen relative to hydrogen of  $1.4 \times 10^{-4}$  and  $3.16 \times 10^{-4}$ , respectively (Sembach et al. 2000). The ISM is embedded in an interstellar radiation field (ISRF) of  $G_0 = 1.7$  in units of Habing (1968), that is in line with Draine (1978). The cosmic ray ionization rate (CRIR) is set to  $3 \times 10^{-17} \text{ s}^{-1}$  with respect to atomic hydrogen. The gas self-gravity as well as the local shielding of the gas from the ISRF is treated with an Octtree-based algorithm described in Wunsch et al. (2018).

For the magnetized runs, we initialize a magnetic field  $\mathbf{B}$  along the  $x$ -direction as

$$B_x = B_{x,0} \sqrt{\rho(z)/\rho_0}, \quad (1)$$

where  $B_{x,0} = 3 \mu\text{G}$  is in accordance to recent observations (e.g. Beck & Wielebinski 2013),  $\rho_0 = 9 \times 10^{-24} \text{ g cm}^{-3}$  (see Walch et al. 2015 for more details), and  $\rho(z)$  is the initial Gaussian density distribution, with  $z$  being the distance from the galactic midplane.

Up to a time  $t_0$  after the beginning of the simulations, supernova (SN) explosions drive turbulence by injecting  $10^{51}$  erg per supernova into the simulation in different possible ways, depending on whether the resolution of the simulation in the point where the SN explodes enables to resolve the Sedov–Taylor phase of the SN or not. The rate at which the supernovae are injected is based on the Kennicutt–Schmidt relation, relating the disc’s surface density (here  $10 M_\odot \text{ pc}^{-2}$ ) with a typical star formation rate surface density. The latter is translated into a supernovae rate by assuming a standard initial mass function (Chabrier 2001). We refer to Walch et al. (2015) and Girichidis et al. (2016) and references therein for details. At  $t_0$  the further injection of background supernovae is stopped to study the evolution of pristine MCs. This does not exclude, however, the possibility that older SN shocks hit the clouds during their evolution. At this point, local gas overdensities i.e. the regions where MCs are about to form, are already visible. We select a few of these ‘zoom-in’ regions and continue the simulations allowing for a resolution up to 0.12 pc in those regions. The typical side length of the zoom-in regions is about 100 pc. We consider two purely hydrodynamical clouds, which we refer to as MC1-HD and MC2-HD, and two magnetohydrodynamical clouds, MC1-MHD and MC2-MHD. The HD runs are described in detail in Seifried et al. (2017) and the MHD runs in Seifried et al. (2019). We emphasize that HD and MHD runs refer to different clouds, they are not just the same clouds with/without external magnetic field included. In MHD runs  $t_0$  is larger than in the HD runs due to the slower dynamical evolution of the MHD clouds (Walch et al. 2015; Girichidis et al. 2016).

We set  $t_0 = 11.9$  Myr for the HD runs and  $t_0 = 16.0$  Myr for the MHD runs. We also run these four clouds with stellar feedback included. We name our runs according to the cloud’s number, whether it is HD or MHD, and whether it has feedback included or not: for instance, MC1-HD-noFB and MC1-HD-FB for non-feedback and feedback runs, respectively. An overview of the simulations features is given in Table 1. In the table, we also show the average density of the clouds  $\rho_0$  at  $t_{\text{evol}} = 0$ . In the feedback runs (see Haid et al. 2019, for a more detailed description), we use sink particles to model the formation and the evolution of stars and, as a consequence, of the ionizing radiation feedback by massive stars. The sinks form when

**Table 1.** Overview of the simulations giving the run name, the zoom time  $t_0$ , the average density  $\rho_0$  at  $t_0$ , the run type (hydrodynamical, HD, or magnetohydrodynamical, MHD), and stellar feedback.

Run name	$t_0$ [Myr]	$\rho_0$ [ $10^{-24}$ g cm $^{-3}$ ]	Run type	Feedback
MC1-HD-noFB	11.9	11.1	HD	No
MC1-HD-FB	11.9	11.1	HD	Yes
MC2-HD-noFB	11.9	8.8	HD	No
MC2-HD-FB	11.9	8.8	HD	Yes
MC1-MHD-noFB	16.0	8.4	MHD	No
MC1-MHD-FB	16.0	8.4	MHD	Yes
MC2-MHD-noFB	16.0	9.5	MHD	No
MC2-MHD-FB	16.0	9.5	MHD	Yes

the gas density exceeds  $1.1 \times 10^{-20}$  g cm $^{-3}$ . Further, the nearby gas has to be in a converging flow, gravitationally bound, Jeans unstable, and in a local gravitational potential minimum. Details on this are provided in Federrath et al. (2010). We also use the sink accretion criteria described there. Next, per  $120 M_\odot$  of accreted mass, a massive star between 9 and  $120 M_\odot$  is created using a random sampling algorithm (Gatto et al. 2017), which follows the initial mass function of Salpeter (1955). The ionizing radiation relative to each star is treated with TreeRay, a method for solving general radiative transfer problems, based on reverse ray-tracing combined with tree-based accelerated integration (Wünsch et al. 2021). As we consider only a short span of stellar evolution, none of the stars have reached the end of their lifetime and have gone off as a supernova yet. The chemical evolution of all HD clouds, as well as MC1-MHD-noFB and MC2-MHD-noFB, in particular for H $_2$  and CO, is reported in Seifried et al. (2020a).

### 3 POST-PROCESSING AND RADIATIVE TRANSFER

Before the actual synthetic emission maps are produced (Section 3.3), we prepare the necessary input data in two steps. The first step is applied to the entire simulation domain (Section 3.1), the second is only applied to regions affected by stellar feedback (Section 3.2). Unless stated otherwise, all the results shown in the remainder of the paper include the post-processing described in the following.

#### 3.1 Data preparation for the radiative transfer

In the first step we apply a pipeline developed by PC Nürnberger<sup>1</sup> to the entire simulation domain. It converts the FLASH simulation data into input files for RADMC-3D (Dullemond et al. 2012, used for the radiative transfer) and incorporates further physical processes: (i) CO freeze-out, (ii) C $^+$   $\rightarrow$  C $^{2+}$  thermal ionization, (iii) splitting of H $_2$  into para- and ortho-H $_2$ , and (iv) setting of the gas microturbulence.

(i) The CO density after the freeze-out post-processing,  $n_{\text{CO},f}$ , is obtained from the original density  $n_{\text{CO}}$  following Glover & Clark (2016) and references therein,

$$n_{\text{CO},f} = n_{\text{CO}} \times \frac{k_{\text{cr}} + k_{\text{therm}}}{k_{\text{cr}} + k_{\text{therm}} + k_{\text{ads}}}, \quad (2)$$

where

$$k_{\text{cr}} = 5.7 \times 10^4 \times \text{CRIR s}^{-1} \text{ molecule}^{-1} \quad (3)$$

<sup>1</sup><https://astro.uni-koeln.de/walch-gassner/downloads/flashpp-pipeline>

is the cosmic rays-induced desorption rate of CO from dust grains,

$$k_{\text{therm}} = 1.04 \times 10^{12} \exp\left(-\frac{960 \text{ K}}{T_{\text{d}}}\right) \text{ s}^{-1} \text{ molecule}^{-1} \quad (4)$$

is the thermal desorption rate. Here,  $T_{\text{g}}$  is the gas temperature and  $T_{\text{d}}$  is the dust temperature. Furthermore,

$$k_{\text{ads}} = 3.44 \times 10^{-18} \sqrt{T_{\text{g}}} (2n_{\text{H}_2} + n_{\text{H}}) \text{ s}^{-1} \text{ molecule}^{-1} \quad (5)$$

is the adsorption rate due to collisions between CO and dust grains.

(ii) The C $^+$   $\rightarrow$  C $^{2+}$  ionization due to collisions induced via thermal motions is implemented using tabulated data from Sutherland & Dopita (1993), who calculate cooling functions for low-density astrophysical plasma in self-consistent 1D models. In cells with a gas temperature  $T_{\text{g}} \geq 2 \times 10^4$  K the C $^+$  density is corrected in order to consider such collisions (see also Franek et al. 2018 for more details).

(iii) We distinguish between the two nuclear spin states of H $_2$ , in which the spins of the nuclei are parallel (ortho – H $_2$ ) or antiparallel (para – H $_2$ ). These are given, following Gerlich (1990) and Rachford et al. (2009), by

$$n(\text{para} - \text{H}_2) = \frac{n_{\text{H}_2}}{9 e^{-170.5 \text{ K}/T_{\text{g}}} + 1} \quad (6)$$

and

$$n(\text{ortho} - \text{H}_2) = n_{\text{H}_2} - n(\text{para} - \text{H}_2). \quad (7)$$

If equations (6) and (7) yield to an ortho-to-para ratio larger than 3, we force  $n(\text{ortho} - \text{H}_2)/n(\text{para} - \text{H}_2) = 3$ , with  $n(\text{ortho} - \text{H}_2) + n(\text{para} - \text{H}_2) = n_{\text{H}_2}$  (see fig. 5 in Gerlich 1990).

(iv) Microturbulence is also included in our radiative transfer calculations. We assume that the microturbulence broadening is as strong as the thermal broadening. This is an assumption we make, motivated by our choice to have the unresolved turbulence with a Mach number of 1 i.e. a transonic turbulence. In any case, as we only analyse moment 0 maps in this work, we expect this choice to have little to no impact on our results. We verify, for a selection of lines of sight and snapshots, that the true line width (due to the gas velocity) is much larger than the line width given by microturbulent and thermal broadening. Therefore, with  $a$  being the line width, we have  $a^2 = a_{\text{therm}}^2 + a_{\text{turb}}^2$ , with

$$a_{\text{therm}} = a_{\text{turb}} = \sqrt{\frac{2k_{\text{B}} T_{\text{g}}}{\mu m_{\text{p}}}}, \quad (8)$$

where  $k_{\text{B}}$  is the Boltzmann constant,  $\mu = 2.3$  is the assumed mean molecular mass of the molecular gas, and  $m_{\text{p}}$  is the proton mass.

#### 3.2 Chemical post-processing of stellar feedback regions

This second data preparation step is only applied to regions affected by stellar feedback to properly model the abundance of C $^+$ . The NL97 chemical network does not contain any higher ionized states of carbon than C $^+$  and the ionization to C $^{2+}$  described before only accounts for thermal ionization. Stellar radiation, however, can cause further ionization of carbon (see e.g. Abel et al. 2005); the stars formed in our simulations have masses greater than, or equal to,  $9 M_\odot$  and are therefore O-type or B-type stars. These stars, whose effective temperature equals or exceeds 24 000 K, emit photons with energies larger than the second ionization energy of carbon of 24.4 eV. It is therefore necessary to remove C $^+$ , which gets further ionized by this radiation, in order to obtain more realistic emission maps of the feedback runs. For this purpose we use a novel approach based on

**Table 2.** Parameter range used for CLOUDY models.

Parameter	Min	Max	# steps
$\rho_g$ [ $\text{g cm}^{-3}$ ]	$10^{-26}$	$10^{-20}$	19
$T_g$ [K]	$10^{1.5}$	$10^{4.5}$	19
$T_*$ [K]	$10^{3.5}$	$10^{5.5}$	21
$E_{\text{ion}}$ [ $\text{erg cm}^{-3}$ ]	$10^{-18}$	$10^{-8}$	21

We run one model for each combination of parameters. Steps are equally spaced in log-scale.

CLOUDY (Ferland et al. 2017), which we describe in detail in the following.

### 3.2.1 CLOUDY data base

We consider four parameters provided by the FLASH simulation data as an input for CLOUDY. The gas density,  $\rho_g$ , the gas temperature,  $T_g$ , the energy density of ionizing photons,  $E_{\text{ion}}$  (converted later to a bolometric luminosity, see below), and the temperature of the star responsible for the ionization,  $T_*$ . In order to avoid to run CLOUDY for each simulation cell, we create a data base beforehand. To do this, we vary the parameters mentioned above over the range of values found in our simulations, summarized in Table 2. We run one CLOUDY model for each possible combination of values, which corresponds to approximately 160 000 models in total.

CLOUDY requires for a source of ionizing photons its bolometric luminosity,  $L_{\text{bol}}$ , and not  $E_{\text{ion}}$ . Therefore, we convert  $E_{\text{ion}}$  into  $L_{\text{bol}}$  as follows. Given a defined spectral luminosity  $L_\nu$  for a star,  $L_{\text{bol}}$  is defined as

$$L_{\text{bol}} = \int_0^\infty L_\nu d\nu. \quad (9)$$

Similarly, we define the ionizing luminosity  $L_{\text{ion}}$  as the spectral luminosity integrated over the frequencies larger than the ionizing frequency of atomic hydrogen,  $\nu_H = 13.6 \text{ eV}/h$ , where  $h$  is the Planck constant,

$$L_{\text{ion}} = \int_{\nu_H}^\infty L_\nu d\nu. \quad (10)$$

Furthermore, assuming that the emission spectrum of the chosen star (see below how we choose the star) is equal to that of a black body with its temperature  $T_*$ ,  $B_\nu(T_*)$ , we have

$$L_{\text{bol}} = L_{\text{ion}} \frac{\int_0^\infty B_\nu(T_*) d\nu}{\int_{\nu_H}^\infty B_\nu(T_*) d\nu}. \quad (11)$$

The treatment of the stellar spectrum as a black body is sufficient for our purposes and we do not expect that our results are significantly affected by this assumption. The energy density of ionizing photons, provided in the FLASH simulation data, is related to the ionizing luminosity (equation 10) via

$$E_{\text{ion}} = \frac{1}{c} \frac{L_{\text{ion}}}{4\pi d^2}, \quad (12)$$

with  $d$  being the distance between the star and the investigated point. Therefore, we can convert  $E_{\text{ion}}$  into  $L_{\text{bol}}$  via

$$L_{\text{bol}} = E_{\text{ion}} \times 4\pi d^2 c \times \frac{\int_0^\infty B_\nu(T_*) d\nu}{\int_{\nu_H}^\infty B_\nu(T_*) d\nu}. \quad (13)$$

In our CLOUDY models we now assume a fixed  $d$  of 100 pc. Hence, equation (13) gives us the luminosity of a *hypothetical* star at a distance of 100 pc, which would provide the exactly same value for  $E_{\text{ion}}$  as the actual star at its real distance due to the attenuation by gas

and dust in between. This approach thus limits the parameter range to be covered by the CLOUDY data base to four dimensions without loss of generality. Furthermore, the cells in our AMR simulations have a size of  $dx = 0.122, 0.244, 0.488, \text{ and } 0.976$  pc. We take  $dx = 0.976$  pc as the depth of the photodissociation region (PDR) in CLOUDY, which automatically includes the results for all smaller cell sizes (see below). In addition, our choice of  $d = 100$  pc assures that  $dx \ll d$ , that is, the CLOUDY models are essentially a plane-parallel PDR which we can then directly map back to the simulation cell.

CLOUDY provides the fractional abundance  $f_{X,\text{cloudy}}$  of the chemical species  $X$  with respect to the total number of hydrogen nuclei i.e.  $f_{X,\text{cloudy}} = n_{X,\text{cloudy}}/n_{\text{H,tot}}$ , as a function of the distance from the edge of the slab. We are interested in the mean value over the cell, to which the slab corresponds. As the length of the (quasi plane-parallel) PDR slab is 0.976 pc, in a next step we average the chemical abundance in the PDR slab from 0 to a depth of  $dx = 0.122, 0.244, 0.488, \text{ and } 0.976$  pc i.e. each CLOUDY model provides now four values of  $f_{X,\text{cloudy}}$ , one for each cell size. Hence, at this point we have a data base covering the full range of relevant physical parameters and possible cell lengths.

### 3.2.2 Calculation of the new $C^+$ abundance

In a next step we now post-process the RADMC-3D input file concerning  $C^+$  on a cell-by-cell basis as follows:

(i) We check whether  $E_{\text{ion}} > 0$ . If this is not the case, we skip the following points and do not post-process the cell. Otherwise,

(ii) In order to estimate which star contributes most to the flux of ionizing photons at the considered cell, we loop over all stars and compute the unattenuated flux  $F_i$  from the  $i$ th star reaching the cell,

$$F_i = L_{\text{bol},i}/4\pi d_i^2. \quad (14)$$

Here,  $d_i$  is the *actual* distance between the cell and the  $i$ th star and  $L_{\text{bol},i}$  the *actual* bolometric luminosity of the  $i$ th star obtained directly from the simulation data.

(iii) We select the  $k$ th star, with temperature  $T_{*,k}$ , for which  $F_k = \max(F_i)$ . For consistency, we check that  $d_k \leq 2d_{\text{min}}$ , with  $d_{\text{min}} = \min(d_i)$ . This is always the case in the simulations presented in this paper. In the following we assume that star  $k$  is solely responsible for all the ionizing photons.

(iv) Next, we take the input values  $\rho_g, T_g, T_{n*,k}, E_{\text{ion}}$ , and the cell size  $dx$  and interpolate the data base for  $f_{C^+,\text{cloudy}}$  created before using LINEARNDINTERPOLATOR, which is part of PYTHON'S NUMPY library, to obtain the updated value  $f_{C^+}$  for the given cell.

(v) Finally, we replace the original  $C^+$  number density of the cell with  $f_{C^+} \times n_{\text{H,tot}}$ , where  $n_{\text{H,tot}}$  is the total hydrogen nuclei number density.

## 3.3 Radiative transfer

We create synthetic emission maps of  $^{12}\text{CO}$  ( $1 \rightarrow 0$ ) at 2600  $\mu\text{m}$ ,  $^{13}\text{CO}$  ( $1 \rightarrow 0$ ) at 2720  $\mu\text{m}$ , and  $[\text{C II}]$  at 158  $\mu\text{m}$  for all eight clouds (see Table 1) at three different evolutionary stages separated by 1 Myr for lines of sight (LOS) along the  $x$ -,  $y$ -, and  $z$ -axis. The emission maps have the same resolution as the highest AMR refinement level i.e. 0.12 pc. The radiative transfer, which is needed to obtain synthetic emission maps of the simulated clouds, is performed using the RADMC-3D software, an open-source, 3D radiative transfer code<sup>2</sup>

<sup>2</sup><http://www.ita.uni-heidelberg.de/~dullemond/software/radmc-3d/>

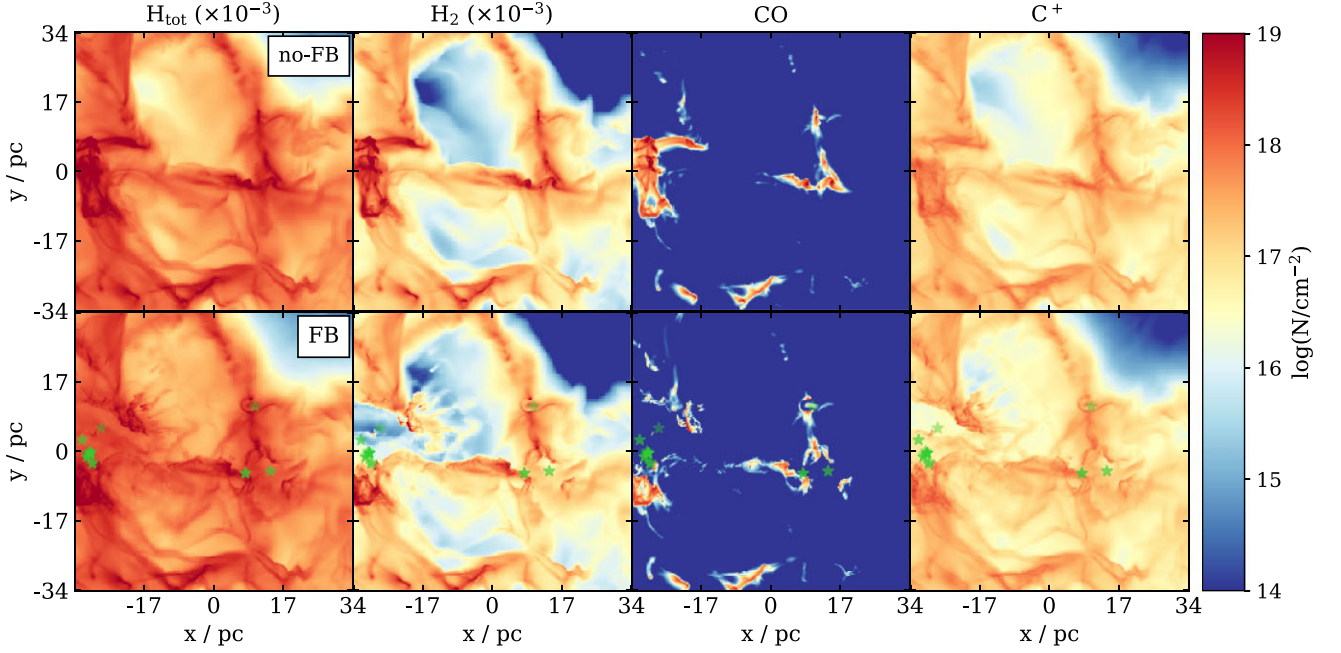


**Figure 1.** Column density of  $H_{\text{tot}}$ ,  $H_2$ , CO, and  $C^+$  (from left to right) of the run MC1-HD-noFB (top row) and MC1-HD-FB (bottom row) at  $t_{\text{evol}} = 4$  Myr along the  $z$ -direction. Green symbols mark the positions where massive stars form. There is an evident nested CO– $C^+$  structure. The  $H_2$  distribution is more diffuse than the CO distribution, which leads to a significant CO-dark  $H_2$  region. Conversely, the  $C^+$  distribution is significantly more diffuse than the  $H_2$  distribution. The impact of stellar radiation is evident when comparing particularly dense regions in the noFB run with the corresponding areas in the FB run, as stellar feedback disperses the cloud.

(Dullemond et al. 2012). We include microturbulence (equation 8) and use the Large Velocity Gradient approximation (LVG; Ossenkopf 1997; Shetty et al. 2011a, b) for calculating the level population. In order to capture the contribution of Doppler-shifted emission, we consider a velocity range of  $\pm 20$  km s $^{-1}$ , centred around the selected rest frequency. We divide this range into 201 equally spaced velocity channels, corresponding to a spectral resolution of  $dv = 0.2$  km s $^{-1}$ , which is well suited for the studied MCs (Franeck et al. 2018).

Performing the radiative transfer calculations using the LVG approximation means that we do not assume local thermal equilibrium. Therefore, we must specify explicitly the collisional rates for CO and  $C^+$ . We take the data from the Leiden Atomic and Molecular Database<sup>3</sup> (LAMDA; Schöier et al. 2005). We consider para- $H_2$ , ortho- $H_2$ , H, and  $e^-$ , as collisional partners for  $C^+$ , and para- $H_2$ , ortho- $H_2$ , H, and He, for CO. As the rates for CO-He and CO-H collisions are not in the LAMDA data base, for this we use the rates from Cecchi-Pestellini et al. (2002) and Walker et al. (2015), respectively. We emphasize that it is essential to include also He and H as collisional partners as it increases the CO luminosity by  $\sim 20$ –30 per cent (Borchert et al. 2022).

We also consider the cosmic microwave background (CMB) using an isotropic black body emission at 2.725 K. This is done both for the level population calculation, where RADMC-3D includes the CMB by default, and for the ray-tracing step. During the analysis of the synthetic emission maps we subtract this background before any other step. Each emission map is centred on a rest frequency  $\nu_0$ . The corresponding antenna temperature for the CMB is given by

$$T_{\text{A,CMB}} = \frac{h\nu_0}{k_{\text{B}}} \frac{1}{e^{h\nu_0/kT} - 1}, \quad (15)$$

<sup>3</sup><https://home.strw.leidenuniv.nl/~moldata/>

where  $h$  is the Planck constant and  $T = 2.725$  K. Considering the CMB background and then subtracting it, has a negligible impact on [C II] emission maps, but it changes the  $^{12}\text{CO}$  and  $^{13}\text{CO}$  intensity in optically thick areas by up to  $\sim 20$  per cent.

## 4 RESULTS

### 4.1 Overview of the simulations

In the following, we refer to the evolution time  $t_{\text{evol}}$  of the clouds as  $t_{\text{evol}} = t - t_0$ , where  $t$  is the time calculated from the very beginning of the SILCC simulation and  $t_0$  is the time when the zoom-in simulation starts (see also Table 1). As mentioned before, the results shown in the following include the post-processing steps described in Section 3 unless stated otherwise.

In Fig. 1 we show in the top row the  $H_{\text{tot}}$ ,  $H_2$ , CO, and  $C^+$  column densities of MC1-HD-noFB at an evolutionary stage of  $t_{\text{evol}} = 4$  Myr along the  $z$ -axis. In the bottom row we show MC1-HD-FB together with the formed stars. The impact of stellar feedback is evident: it is possible to identify two regions of star formation where stellar radiation disperses the cloud. This is particularly clear when looking at the  $H_2$  and CO maps, since the higher temperature and the stellar radiation lead to the dissociation of these molecules. Stellar radiation has also an impact on  $C^+$  by further ionizing it to  $C^{2+}$  (see Section 3.2). Furthermore, comparing the  $H_2$  column density with the carbon-bearing species maps, shows that the CO distribution is significantly more compact than the  $H_2$  distribution, which leads to the presence of CO-dark  $H_2$  regions (see Seifried et al. 2020a for details on this). The  $C^+$  distribution is significantly more diffuse than the CO distribution, leading to a clearly visible nested CO– $C^+$  structure.

Fig. 2 shows the change in CO,  $C^+$ , and  $H_2$  mass fraction as a function of time for the simulated clouds in the zoom-in

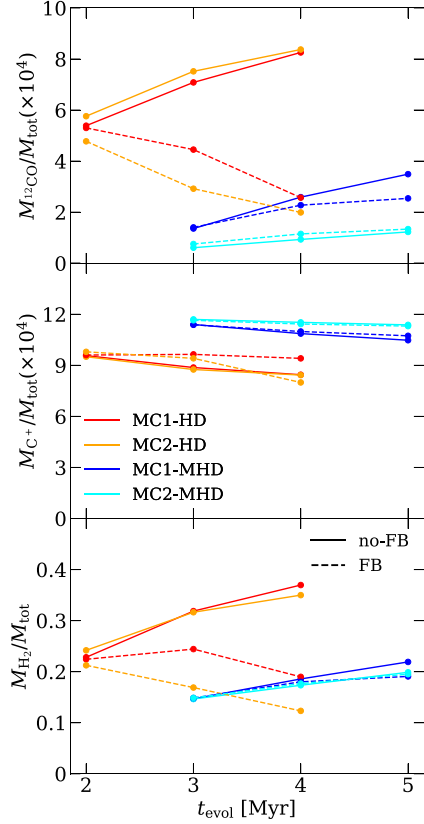


**Figure 2.** Mass fraction, with respect to total mass, of  $^{12}\text{CO}$ ,  $\text{C}^+$ , and  $\text{H}_2$  (from top to bottom) as a function of time for all four clouds, represented in different colours. The noFB runs are plotted with solid lines, and FB runs in dashed lines. The CO mass rises with time, whereas the  $\text{C}^+$  mass slowly decreases. The MHD clouds evolve more slowly than the HD clouds: at given  $t_{\text{evol}}$ , the  $\text{H}_2$  and CO abundances are significantly lower in the MHD case than in the HD case (no-FB runs). Stellar feedback disperses the densest parts of the clouds, where stars form, thus decreasing the mass of CO and  $\text{H}_2$  over time.

regions, using selected snapshots separated by 1 Myr in time. In our simulations,  $M_{^{13}\text{CO}}$  (not shown here) is fixed to 1/69 of  $M_{^{12}\text{CO}}$  (Wilson 1999). For runs without feedback, the CO and  $\text{H}_2$  abundances rise with time, and the  $\text{C}^+$  abundance slowly decreases. Both the HD and MHD clouds follow the same trend, but the MHD clouds evolve more slowly: this can be seen, for instance, when considering the  $\text{H}_2$  and CO mass fractions for the HD-noFB and MHD-noFB clouds at a given  $t_{\text{evol}}$ . These are significantly lower in the MHD case and this is due to the slower formation of dense structures in the clouds, because the magnetic field has a stabilizing effect for densities below a few  $100 \text{ cm}^{-3}$  (Seifried et al. 2020a, b). We point out that this result is not a consequence of the choice of  $t_0$ : even though this is indeed somewhat arbitrary, the average densities of the clouds at  $t_0$  are comparable (see Table 1). However, in the presence of magnetic fields, the density contrast i.e. overdensities are less pronounced (see Ganguly et al. 2022). We test this by calculating the density dispersion for each cloud at  $t_{\text{evol}} = 0$  (not shown). We find that the dispersion is about 75 percent larger in HD clouds than in MHD clouds. Therefore even though the average density does not change, our MHD clouds form molecules more slowly than HD clouds as the molecule formation time-scale (in well-shielded gas with negligible dissociation) scales with the local density.

Stellar feedback reduces the amount of CO and  $\text{H}_2$  from the onset of star formation. For the MHD clouds this effect is less pronounced:

due to their slower formation of molecular regions (Fig. 2) the overall stellar mass and luminosity is lower compared to the HD clouds as well (as stars form in the dense cores). This is particularly true for MC2-MHD and, to a smaller extent, for MC1-MHD. We show in a subsequent paper (Ebagezio et al., in preparation) that the stellar luminosity is a robust parameter to assess the importance of feedback on a cloud. The total amount of  $\text{C}^+$  is only marginally affected by stellar feedback (due to a partial conversion into  $\text{C}^{2+}$ ), although feedback results in a different distribution of  $\text{C}^+$  (see Fig. 1, right column).

## 4.2 Synthetic emission maps

Next, we analyse the emission maps for the same snapshots as in Fig. 2. In Fig. 3 we show the integrated intensity maps of the  $^{12}\text{CO}$ ,  $^{13}\text{CO}$ , and  $[\text{C II}]$  lines of MC1-HD-noFB (top row) and MC1-HD-FB (bottom row) at  $t_{\text{evol}} = 4 \text{ Myr}$ , which corresponds to the column density maps shown in Fig. 1. Again, a nested CO -  $[\text{C II}]$  structure is evident, and stellar feedback removes the CO emission from the expanding bubbles and strongly increases the  $[\text{C II}]$  emission, in particular from the rims of the bubbles.

Next, we calculate the total luminosity  $L$ . For this, we first sum the intensity of all pixels to obtain the integrated intensity. Then,  $L$  is given by

$$L = 4\pi d^2 F, \quad (16)$$

where  $d$  is the distance of the cloud and  $F$  is the total flux derived from the integrated intensity map by adding up the contributions from the total number of pixels,  $n$ :

$$F = \sum_{i=1}^n I_i A_{\text{pixel}}. \quad (17)$$

Here,  $A_{\text{pixel}}$  is the area of the pixels in steradians given by

$$A_{\text{pixel}} = \left( \arctan \left( \frac{a}{d} \right) \right)^2, \quad (18)$$

with  $a$  being the side length of the pixel. We note that, due to the small angle approximation, for  $a/d \ll 1$  the choice of  $d$  is practically irrelevant.

We show the values of  $L$  calculated for the three different LOS in Fig. 4. Optical thickness plays an important role for  $L_{^{12}\text{CO}}$ , indicated by the fact that the values for the same cloud, but different LOS, differ by up to a factor of a few, whereas in the optically thin case they should be identical. This is also shown by the fact that changes in  $L_{^{12}\text{CO}}$  (e.g. for MC1-HD-noFB). Conversely, the measured  $L_{^{13}\text{CO}}$  is less affected by optical thickness: the difference in luminosity for the different LOS is lower than for  $^{12}\text{CO}$ , and  $L_{^{13}\text{CO}}$  changes coherently with  $M_{\text{CO}}$ .

Stellar feedback significantly increases  $L_{[\text{C II}]}$  compared to the noFB runs by a factor of 2–7. Only MC2-MHD-FB, which forms the least stellar mass among the clouds we investigate ( $41.9 M_{\odot}$  at  $t_{\text{evol}} = 5 \text{ Myr}$  compared to a maximum of  $546.2 M_{\odot}$  in MC2-HD-FB at 4 Myr), does not show a significant increase in  $L_{[\text{C II}]}$ . In contrast,  $M_{\text{C}^+}$  is practically unchanged between noFB and FB runs (Fig. 2, middle panel). The increase in  $L_{[\text{C II}]}$  is a consequence of the stellar radiation, which heats up the gas and excites the  $\text{C}^+$  ions; we find that the excitation temperature of  $[\text{C II}]$  is overall significantly higher in FB (up to 1000 K) than in noFB runs (hardly more than 50 K). In consequence,  $L_{[\text{C II}]}$  increases for the FB runs despite a comparable amount of  $\text{C}^+$  mass between FB and noFB. Most of the  $[\text{C II}]$  luminosity in these runs comes from the rims of the H II

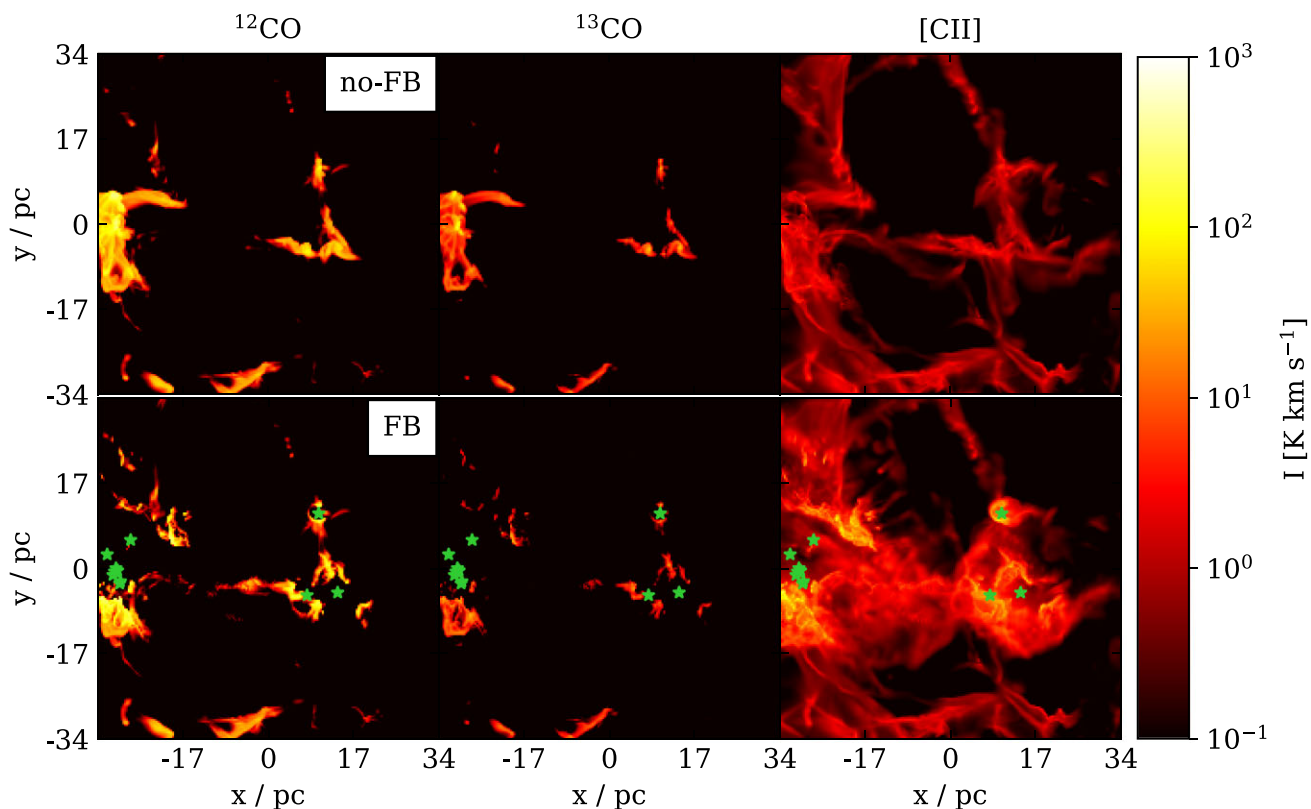


**Figure 3.** From left to right: Integrated emission maps of  $^{12}\text{CO}$  ( $1 \rightarrow 0$ ),  $^{13}\text{CO}$  ( $1 \rightarrow 0$ ), and  $[\text{C II}]$  of MC1-HD without feedback (top row) and with feedback (bottom row) at  $t_{\text{evol}} = 4$  Myr. The CMB background has been subtracted. A nested CO– $[\text{C II}]$  is evident in both clouds. H II regions around stars devoid of any or most of the emission are visible in both the  $[\text{C II}]$  and in CO maps.  $[\text{C II}]$  intensity is enhanced by an order of magnitude in the rims of the H II regions with respect to the brightest areas in the non-feedback map.

bubbles, as shown for instance in Fig. 3. Pineda et al. (2013, 2014) claim that 34–70 per cent of the  $[\text{C II}]$  emission is related to feedback. The factor of 2–7 which we observe for the increase of the  $[\text{C II}]$  luminosity corresponds to a contribution of 50–85 per cent due to the role of stellar feedback, in rough agreement with the estimate of the aforementioned authors. Moreover, we find that the longer star formation proceeds, the more  $[\text{C II}]$  increases, thus having an increasingly more important effect on  $L_{[\text{C II}]}$ .

### 4.3 Feedback-driven $[\text{C II}]$ bubbles

As seen in Fig. 3, stellar feedback drives some bubbles also visible in  $[\text{C II}]$ , which we investigate in more detail now. For this purpose, in Fig. 5 we show some examples of H II regions at different evolutionary stages. Stars are superimposed and are characterized with different colours and size according to their age and temperature. In Fig. A1 we also show the emission maps of the same regions obtained without operating the post-processing described in Section 3.2. These exhibit a much higher emission coming from the inner regions supporting the importance of the post-processing. We find that some structures become more evident after the post-processing. This is the case of pillars, which can be easily recognised in the maps of MC2-HD-FB.

In Fig. 6 we summarize the importance of this post-processing step. The total  $[\text{C II}]$  luminosity decreases by up to 60 per cent if the  $\text{C}^+$  within the H II regions is post-processed compared to the less realistic non-post-processed case. In general, differences are larger at later evolutionary stages, as the stellar mass and thus stellar

radiation intensity increase over time. Hence, the consideration of higher ionization states of carbon is crucial to obtain accurate  $[\text{C II}]$  intensities stemming from H II regions (Spitzer 1978).

The bubbles shown in Fig. 5 are, from left to right, progressively more evolved. Young bubbles are small in size (a few pc) and their inner part is bright in  $[\text{C II}]$  in comparison with more evolved clouds. These evolved bubbles are, in contrast, larger (a few 10 pc) and  $[\text{C II}]$ -dark. This is due to the following mechanism. First, more evolved bubbles contain more stars and, as a consequence, more stellar luminosity and ionizing radiation. At late evolutionary stages the total ionizing radiation present in the clouds is several orders of magnitude larger than at earlier stages. The amplitude of this increase, however, strongly depends on the snapshots and clouds chosen: for instance, it increases by eight orders of magnitude in MC1-HD between  $t_{\text{evol}} = 2$  and 4 Myr, and by two orders of magnitude in the same interval in MC2-HD. This large ionizing radiation makes the  $\text{C}^+ \rightarrow \text{C}^{2+}$  photoionization important in evolved bubbles: as we already mentioned, including this reduces the  $[\text{C II}]$  luminosity in MCs by up to 60 per cent. The impact of this can be seen in Fig. A1, where the same H II regions, with and without post-processing, are shown. In addition, the stellar feedback clears out the H II region, pushing dust and gas away from the stars. A more detailed analysis of the evolution of the  $[\text{C II}]$  luminosity within H II regions is carried out in Ebagezio et al. (in preparation).

At the rims of the bubbles, the  $[\text{C II}]$  emission is enhanced when compared to even the brightest regions of the noFB runs (Fig. 3). This is due to the strong excitation of the  $[\text{C II}]$  line, as we show in detail in a subsequent paper (Ebagezio et al., in preparation). We emphasize

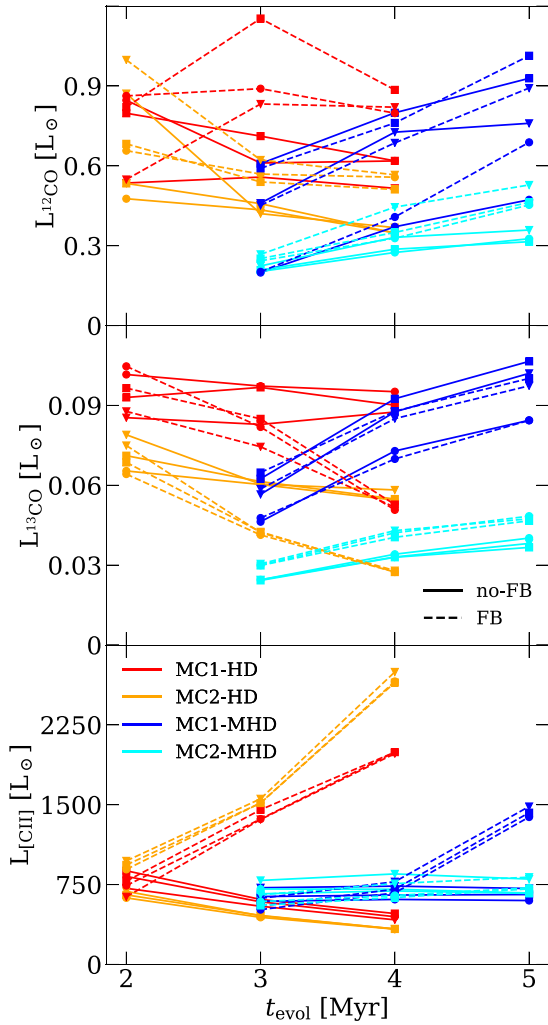


**Figure 4.** Total luminosity of  $^{12}\text{CO}$ ,  $^{13}\text{CO}$ , and  $[\text{C II}]$  for the investigated clouds. Circles, squares, and triangles indicate values along  $z$ -,  $y$ -, and  $x$ -axis, respectively. The differences in the evolution of  $L_{12\text{CO}}$  and  $L_{13\text{CO}}$ , together with the smaller scatter of  $L_{13\text{CO}}$  among the different lines of sight (LOS) for the same cloud, indicate that  $^{12}\text{CO}$  is more affected from optical thickness than  $^{13}\text{CO}$ . The significant increase of  $L_{[\text{C II}]}$  in the feedback runs is a consequence of the enhanced excitation temperature of  $\text{C}^+$  due to stellar feedback. This is not the case for MC2-MHD as the stellar feedback plays a minor role for this cloud.

that our findings are in excellent agreement with  $[\text{C II}]$  bubbles with enhanced emission at the rims and a lack of emission inside found recently in a number of observations (see e.g. Pabst et al. 2019; Luisi et al. 2021; Tiwari 2021).

#### 4.4 The $X_{\text{CO}}$ and $X_{[\text{C II}]}$ factors

The  $X_{\text{CO}}$  factor has been widely studied in literature (see e.g. Scoville et al. 1987; Dame et al. 1993; Strong & Mattox 1996; Melchior et al. 2000; Lombardi et al. 2006; Nietten et al. 2006; Smith et al. 2012; Bolatto et al. 2013; Ripple et al. 2013). It is defined as

$$X_{\text{CO}} = \frac{N_{\text{H}_2}}{W_{12\text{CO}}}, \quad (19)$$

where  $N_{\text{H}_2}$  is the  $\text{H}_2$  column density, generally expressed in  $\text{cm}^{-2}$ , and  $W_{12\text{CO}}$  the line-integrated intensity, summed over the whole image, expressed in  $\text{K km s}^{-1}$ . Here we calculate  $X_{\text{CO}}$  as the average quantity

over the entire cloud. It allows to assess the  $\text{H}_2$  mass of a cloud, given the intensity of the  $^{12}\text{CO}$  ( $1 \rightarrow 0$ ) transition. The typical  $X_{\text{CO}}$  value for the Milky Way is  $2 \times 10^{20} \text{ cm}^{-2} \text{ K}^{-1} \text{ km}^{-1} \text{ s}$  (e.g. Bolatto et al. 2013). We analogously define the  $X_{[\text{C II}]}$  factor as

$$X_{[\text{C II}]} = \frac{N_{\text{H}_2}}{W_{[\text{C II}]}}. \quad (20)$$

In Fig. 7 we show both factors for our simulations plotted against the mass fraction of  $\text{H}_2$  (see Seifried et al. 2020a, for a plot against  $t_{\text{evol}}$ ). We calculate them under the assumption of unresolved clouds i.e. we first integrate the  $\text{H}_2$  column density and the  $\text{CO}$ , or  $[\text{C II}]$ , intensity over the entire area of the zoom-in regions, no matter whether in some pixels the intensity is beyond a minimum observable threshold, and then take the ratio of both values.

There is a significant scatter of  $X_{\text{CO}}$  (left-hand panel of Fig. 7) around the reference value for the Milky Way. In our clouds it spans from  $\sim 0.5$  to  $\sim 4.5 \times 10^{20} \text{ cm}^{-2} \text{ K}^{-1} \text{ km}^{-1} \text{ s}$ . This scatter occurs among different clouds, but also to a smaller extent for the same clouds among different LOS and different  $t_{\text{evol}}$ . It can in parts be attributed to the fact that a larger  $\text{CO}$  optical thickness leads to a higher  $X_{\text{CO}}$  factor, as the  $\text{CO}$  intensity does not increase coherently with the  $\text{H}_2$  mass. Furthermore, differences occur between feedback and non-feedback runs, in particular for HD clouds. Stellar feedback lowers the  $X_{\text{CO}}$  factor, as it both slightly enhances the  $\text{CO}$  emissivity and reduces the  $\text{H}_2$  mass (see Figs 2 and 4).

Moreover, we cannot identify a clear correlation between  $X_{\text{CO}}$  and the time evolution, respectively, the  $\text{H}_2$  mass fraction of the clouds. We attribute this to the presence of ‘ $\text{CO}$ -dark’ regions i.e. molecular gas regions with low or no  $\text{CO}$ . The amount of  $\text{CO}$ -dark gas is highly variable in different clouds. As discussed in more detail in Seifried et al. (2020a), the  $\text{CO}$ -dark gas fractions in our MCs range from 40 to 95 per cent. Indeed, we find that the higher the  $\text{CO}$ -dark gas fraction, the higher is  $X_{\text{CO}}$  e.g. for MC1-HD-noFB and MC2-HD-noFB the  $\text{CO}$ -dark gas fraction is  $\sim 40$  per cent and  $X_{\text{CO}} = 1 - 2 \times 10^{20} \text{ cm}^{-2} \text{ K}^{-1} \text{ km}^{-1} \text{ s}$ , whereas for MC1-MHD-noFB and MC2-MHD-noFB the  $\text{CO}$ -dark gas fraction is 60–95 per cent, and the associated  $X_{\text{CO}}$  is  $1.5 - 4 \times 10^{20} \text{ cm}^{-2} \text{ K}^{-1} \text{ km}^{-1} \text{ s}$ . We note that the  $X_{\text{CO}}$  values calculated in Seifried et al. (2020a) are slightly different, as there they were calculated considering only the pixel with a  $\text{CO}$  intensity above a minimum threshold of  $0.1 \text{ K km s}^{-1}$ .

The  $X_{[\text{C II}]}$  factor (right-hand panel of Fig. 7) exhibits a lower scatter between the different LOS of the same cloud, which we attribute to the somewhat lower optical depths in the case of  $[\text{C II}]$ . Nevertheless, the scatter among different clouds is again significant, with  $X_{[\text{C II}]}$  values ranging from 0.5 to  $12 \times 10^{20} \text{ cm}^{-2} \text{ K}^{-1} \text{ km}^{-1} \text{ s}$ . This means that such  $X_{[\text{C II}]}$  is far from being constant and therefore it is difficult to use it as a reliable conversion factor to obtain the  $\text{H}_2$  mass. Also Franek et al. (2018) claim that  $[\text{C II}]$  is not a good tracer of molecular hydrogen, as most of the  $[\text{C II}]$  intensity comes indeed from atomic hydrogen gas, and not from molecular part. Hence, the monotonic increase in  $X_{[\text{C II}]}$  for the noFB runs is mainly due to the increase in  $\text{H}_2$  mass, while the  $[\text{C II}]$  luminosity stemming from the outskirts of the clouds remains largely constant (see Figs 2 and 4). The FB runs, conversely, do not exhibit a clear relation because the stellar feedback both inhibits the formation of  $\text{H}_2$  (Fig. 2) and enhances the  $[\text{C II}]$  intensity (Fig. 4).

#### 4.5 The global $\text{CO}/[\text{C II}]$ line ratio

The large scatter in  $X_{\text{CO}}$  makes it difficult to use it to reliably estimate the  $\text{H}_2$  mass for individual clouds (Bolatto et al. 2013; Madden et al. 2020; Seifried et al. 2020a; Hu et al. 2022). We therefore consider

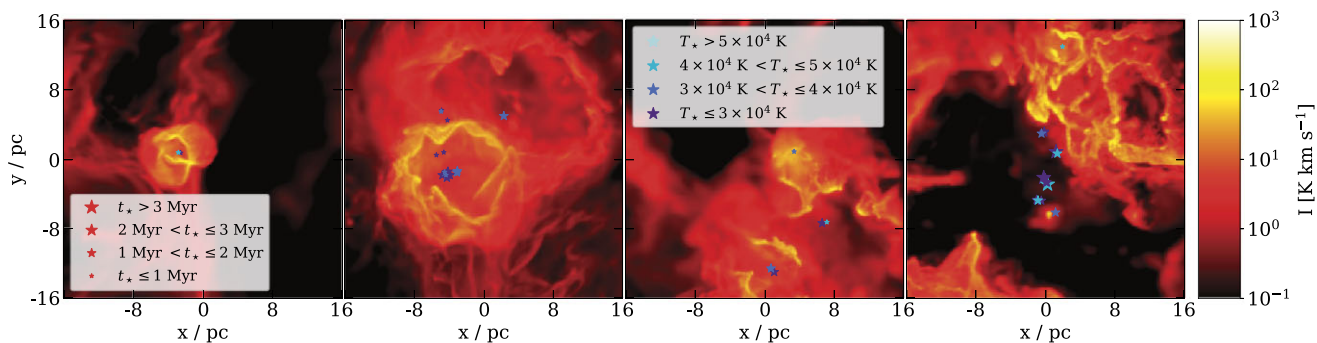


**Figure 5.** H II regions at different evolutionary stages as seen in [C II]. The individual snapshots are taken from different clouds: from left to right, (i) MC2-MHD-FB,  $t_{\text{evol}} = 5$  Myr, LOS along the  $z$ -axis; (ii) MC1-MHD-FB,  $t_{\text{evol}} = 5$  Myr, LOS along the  $y$ -axis; (iii) MC1-HD-FB,  $t_{\text{evol}} = 4$  Myr, LOS along the  $y$ -axis, and (iv) MC2-HD,  $t_{\text{evol}} = 4$  Myr, LOS along the  $x$ -axis. The bubbles are ordered, from left to right, from the youngest to the oldest evolutionary stage. Stars formed are superimposed and plotted with different sizes and colours according to their age and temperature. We find that the larger and [C II]-darker bubbles are associated with older stars, whereas smaller and brighter bubbles correspond to younger stars.

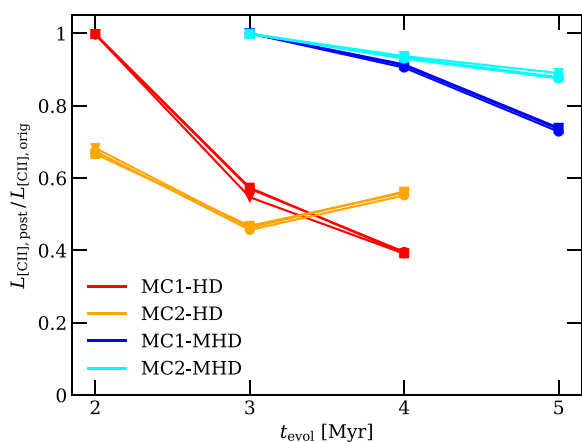


**Figure 6.** Ratio between the total luminosity of [C II] of the post-processed data,  $L_{[\text{CII}],\text{post}}$ , and the original data,  $L_{[\text{CII}],\text{orig}}$ . Circles, squares, and triangles indicate values along  $z$ -,  $y$ -, and  $x$ -axis, respectively. Post-processing the simulation data removes up to 60 per cent of the [C II] luminosity, especially at later stages where feedback becomes more important. Hence, it is essential to obtain reliable [C II] emission maps.

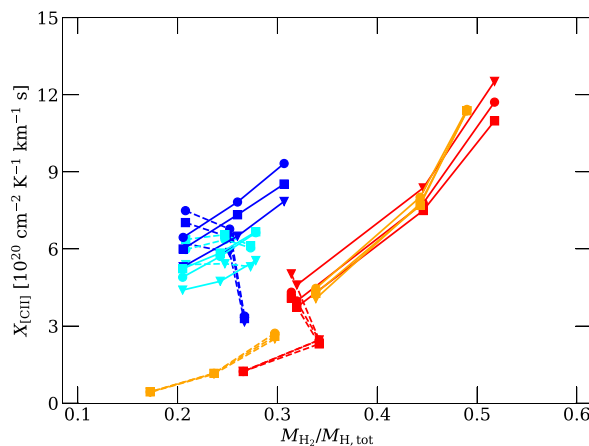
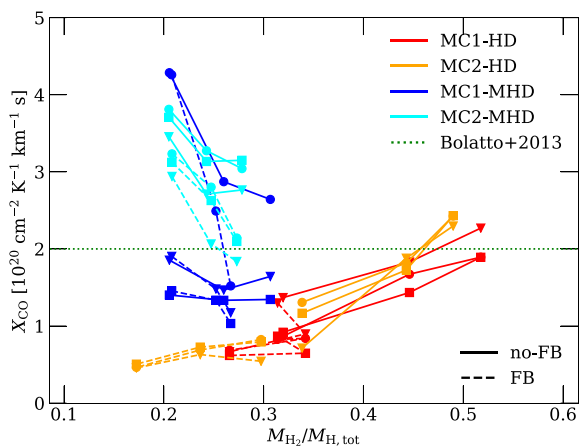


**Figure 7.**  $X_{\text{CO}}$  (left) and  $X_{[\text{CII}]}$  (right) of our simulated clouds as a function of the  $\text{H}_2$  mass fraction. Circles, squares, and triangles indicate values along  $z$ -,  $y$ -, and  $x$ -axis, respectively. Regarding  $X_{\text{CO}}$ , we find a significant scatter among the different clouds and in time around the reference value for the Milky Way of  $2 \times 10^{20} \text{ cm}^{-2} \text{ K}^{-1} \text{ km}^{-1} \text{ s}$  (dotted line). A similar scatter is found for  $X_{[\text{CII}]}$  as well. We see an increase of  $X_{[\text{CII}]}$  with  $M_{\text{H}_2}/M_{\text{H,tot}}$  for the non-FB runs, whereas the FB runs show no clear trend.

another possible estimator: We take the total luminosities integrated over the entire cloud,  $L_{12\text{CO}}$ ,  $L_{13\text{CO}}$ , and  $L_{[\text{CII}]}$ , and investigate the relation between  $L_{12\text{CO}}/L_{[\text{CII}]}$ ,  $L_{13\text{CO}}/L_{[\text{CII}]}$ , and the  $\text{H}_2$  mass fraction of the clouds,  $M_{\text{H}_2}/M_{\text{H,tot}}$ .

Fig. 8 shows  $L_{12\text{CO}}/L_{[\text{CII}]}$  and  $L_{13\text{CO}}/L_{[\text{CII}]}$  as a function of time (top row) and as a function of the  $\text{H}_2$  mass fraction  $M_{\text{H}_2}/M_{\text{H,tot}}$  (bottom row). In Appendix A (Figs A2 and A4) we also show the line ratios as a function of the  $\text{H}_2$  mass and the [C II]/CO ratio calculated with luminosities given in units of  $\text{erg s}^{-1} \text{ cm}^{-2}$  in order to allow for an easier comparison with observational literature. We note that we relate the luminosity ratio to  $M_{\text{H}_2}/M_{\text{H,tot}}$  rather than  $M_{\text{H}_2}$ , as the latter depends on the size of the cloud i.e. it is an extensive quantity and not an intensive one as the mass fraction.

We find that different LOS of the same cloud typically have significantly different  $L_{12\text{CO}}/L_{[\text{CII}]}$  values with the exception of MC2-MHD (for both FB and noFB). The scatter is of the order of a factor of a few in some snapshots: for instance, in MC2-HD-noFB at  $t_{\text{evol}} = 4$  Myr,  $L_{12\text{CO}}/L_{[\text{CII}]}$  is  $\sim 1.5$  for the LOS along the  $z$ -axis, but it is  $\sim 4.3$  along the  $x$ -axis. Considering  $^{13}\text{CO}$  instead of  $^{12}\text{CO}$  considerably reduces the scatter between different LOS. The same snapshot gives  $L_{13\text{CO}}/L_{[\text{CII}]}$   $\simeq 0.4$  along the  $z$ -axis and 0.5 along the  $x$ -axis. As discussed, this is due to the lower optical depth of

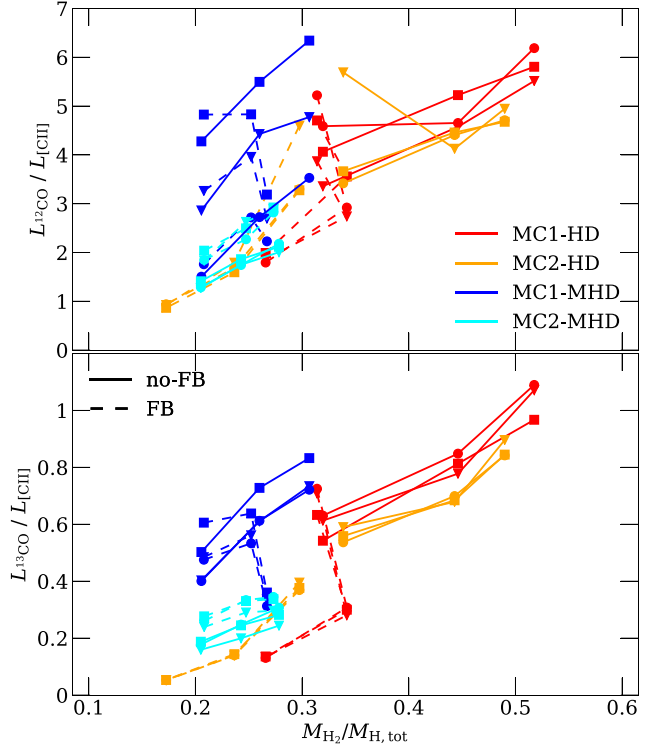
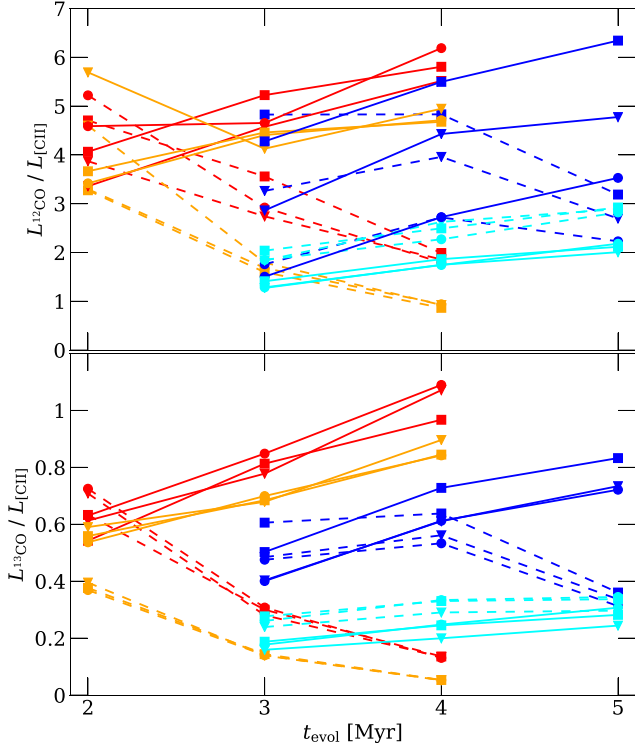


**Figure 8.**  $L_{12\text{CO}}/L_{[\text{CII}]}$  (top row) and  $L_{13\text{CO}}/L_{[\text{CII}]}$  (bottom row) as a function of  $t_{\text{evol}}$  (left column) and  $M_{\text{H}_2}/M_{\text{H,tot}}$  (right column). For all noFB runs the line ratio increases with  $t_{\text{evol}}$ . For all FB runs it decreases, with the only exception of MC2-MHD-FB, which has less dense gas. Altogether, there is no clear trend of the luminosity ratio with either  $t_{\text{evol}}$  and  $M_{\text{H}_2}/M_{\text{H,tot}}$ . In addition, there is a large scatter for a given evolutionary stage. The scatter among different LOS is reduced when considering  $^{13}\text{CO}$ , due to its smaller optical thickness.

$^{13}\text{CO}$  with respect to  $^{12}\text{CO}$  (Borchert et al. 2022). Indeed, we would expect identical values for different LOS if the lines were completely optically thin. To a good approximation, this is the case for the snapshots which have very low CO mass fraction i.e. MC2-MHD, which is a more diffuse cloud, and MC1-HD-FB and MC2-HD-FB at  $t_{\text{evol}} = 4$  Myr (see Fig. 2), where stellar feedback has dispersed most of the dense regions.

We also observe a relevant scatter of a factor of up to a few in the line ratios among different clouds for a selected  $\text{H}_2$  mass fraction. This is a consequence of the different structures and properties of the clouds and does not change significantly when considering  $^{12}\text{CO}$  or  $^{13}\text{CO}$ . For instance, for  $M_{\text{H}_2}/M_{\text{H,tot}} \simeq 0.3$ ,  $L_{12\text{CO}}/L_{[\text{CII}]}$  ranges from 2 to 6 and  $L_{13\text{CO}}/L_{[\text{CII}]}$  from 0.2 to 0.8. As we discuss in detail in the following, we do not observe a systematic relation between higher/lower line ratios (at fixed  $\text{H}_2$  mass fraction) and the presence/absence of magnetic fields or stellar feedback.

Stellar feedback has an impact on the evolution of the line ratio: if no feedback is considered, the line ratios increase with  $t_{\text{evol}}$ : this can be seen clearly for the HD runs, and, even though less evidently, also in the MHD runs. Conversely, including stellar feedback causes a decreasing ratio over time for the same clouds. This trend is less pronounced for MC2-MHD because it is less developed and therefore the stellar feedback has a smaller impact.

The luminosity ratios as a function of  $M_{\text{H}_2}/M_{\text{H,tot}}$  exhibit an overall increasing relation for noFB runs (apart from optical thickness effects). On the other hand, for the FB clouds, there is no clear trend any more. This is a consequence of the fact that both the  $\text{H}_2$  mass fraction (Fig. 2) and the CO/[C II] luminosity ratio (Fig. 8, left-hand side plot) decrease with  $t_{\text{evol}}$ , but with different slopes, making their reciprocal relation non-trivial.

In summary, there is no clear trend of the luminosity ratios with both  $t_{\text{evol}}$  and  $M_{\text{H}_2}/M_{\text{H,tot}}$ . This implies that it is not possible to quantitatively assess an age or evolutionary stage of a cloud by measuring a certain line ratio value. Moreover, there is a large scatter among different LOS and different clouds. We refer to Section 5.1 for a further discussion about the implications of these findings and a comparisons with recent observational works.

## 4.6 Analysis of single pixels

### 4.6.1 The intensity–column density relation

Next, we investigate – pixel by pixel – the relation between the intensity  $I$  (in  $\text{K km s}^{-1}$ ) of  $^{12}\text{CO}$ ,  $^{13}\text{CO}$ , and [C II] and the column density  $N$  of  $^{12}\text{CO}$ ,  $^{13}\text{CO}$ ,  $\text{C}^+$ , and  $\text{H}_2$ . It is, however, useful to analyse the relation between the CO and  $\text{C}^+$  column density with the  $\text{H}_2$  column density first. This is done in Fig. 9, where we show this for MC2-HD at  $t_{\text{evol}} = 4$  Myr (the results for other snapshots and clouds are similar). Each line represents the mean value of  $N_X$  for a given  $N_{\text{H}_2}$ -bin for the selected snapshot. The  $\text{C}^+$  column density increases with increasing  $N_{\text{H}_2}$  for  $N_{\text{H}_2} \lesssim 10^{21} \text{ cm}^{-2}$ , and is roughly constant for larger  $N_{\text{H}_2}$ . The CO column density is increasing superlinearly with  $N_{\text{H}_2}$  below  $N_{\text{H}_2} \sim 10^{21}$ , and changes to a roughly linear relation above this value. This means that most of carbon is in form of CO for  $N_{\text{H}_2} \gtrsim 10^{21}$ . We do not note important differences between FB and noFB runs.

The relation between  $I_{12\text{CO}}$ ,  $I_{13\text{CO}}$ ,  $I_{[\text{CII}]}$ , and  $N_{\text{H}_2}$  is shown in Fig. 10, where  $I_{12\text{CO}}$  (left-hand panel),  $I_{13\text{CO}}$  (middle panel), and  $I_{[\text{CII}]}$  (right-hand panel) are plotted as a function of  $N_{\text{H}_2}$ . Each line represents the mean value of  $I$  for a given  $N_{\text{H}_2}$ -bin for the

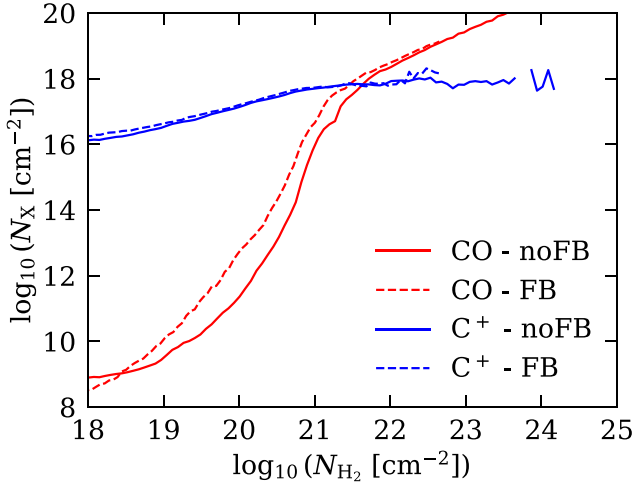


**Figure 9.**  $N_{\text{CO}}$  and  $N_{\text{C}^+}$  as a function of  $N_{\text{H}_2}$  for MC2-HD at  $t_{\text{evol}} = 4$  Myr. Lines (solid for noFB runs and dashed for FB runs) represent the mean values for each  $N_{\text{H}_2}$ -bin. The slope of the curves changes at  $N_{\text{H}_2} \simeq 10^{21} \text{ cm}^{-2}$ . In particular,  $N_{\text{C}^+}$  is roughly constant for  $N_{\text{H}_2} \gtrsim 10^{21} \text{ cm}^{-2}$ .

selected snapshot. Snapshots corresponding to different  $t_{\text{evol}}$  for the same cloud are plotted with the same colour, and therefore are not distinguished here. We plot only the data resulting from the integration along the  $z$ -direction. However, we obtain qualitatively and quantitatively similar results when considering the  $x$ - or the  $y$ -direction. We note that the large scatter at very low and very high  $N_{\text{H}_2}$  is due to the low number of pixels in these regimes. For comparison (see later), for  $I_{[\text{C II}]}$  we also plot the observational data from Hall et al. (2020) for the Perseus Giant Molecular Cloud (GMC; black squares).

The curves of  $I_{12\text{CO}}$  and  $I_{13\text{CO}}$  exhibit a change in slope at  $N_{\text{H}_2} \sim 10^{21} \text{ cm}^{-2}$ . This change is more sudden in the  $^{12}\text{CO}$  than in the  $^{13}\text{CO}$  case. In order to explain the observed shapes of the  $I_{\text{CO}} - N_{\text{H}_2}$  curves, we consider the optical thickness  $\tau_{\text{CO}}$  and the excitation temperature  $T_{\text{ex}}$  of the transition line as a function of  $N_{\text{H}_2}$ . We show the corresponding plots in Appendix A in Fig. A3 and just summarize the main findings here.

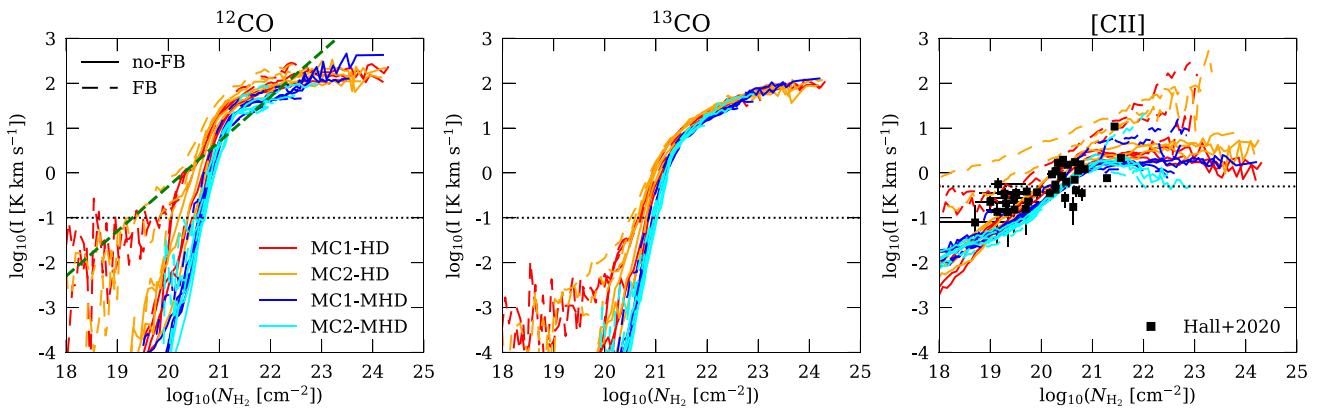


**Figure 10.**  $I_{12\text{CO}}$ ,  $I_{13\text{CO}}$ , and  $I_{[\text{C II}]}$  (from left to right) as a function of the column density of  $\text{H}_2$  seen along the  $z$ -axis. Lines (solid for noFB runs and dashed for FB runs) represent the mean values for each  $N_{\text{H}_2}$ -bin. Snapshots at different  $t_{\text{evol}}$ , for a given cloud, are plotted with the same colour. The dotted, horizontal lines represent realistic observable limits for CO and [C II], which we set to 0.1 and 0.5  $\text{K km s}^{-1}$ , respectively. The dashed, green line in the top left-hand panel represents the  $X_{\text{CO}}$  reference value given by Bolatto et al. (2013) and the black squares on the right plot represent the observational data from Hall et al. (2020). All curves tend to flatten for  $N_{\text{H}_2} \gtrsim 10^{21} \text{ cm}^{-2}$ . For [C II], this is mainly due to the transition from  $\text{C}^+$  to CO at  $N_{\text{H}_2} \sim 10^{21} \text{ cm}^{-2}$  (see Fig. 9). For CO, it is related to the slope change in the  $N_{\text{CO}} - N_{\text{H}_2}$  curve at  $N_{\text{H}_2} \sim 10^{21} \text{ cm}^{-2}$  (again, see Fig. 9), and in addition, for  $^{12}\text{CO}$ , to optical depth effects.

We find that the  $^{12}\text{CO}$  transition becomes optically thick at  $N_{\text{H}_2} \simeq 10^{21} \text{ cm}^{-2}$ . This and our findings that the increase of  $N_{\text{CO}}$  with  $N_{\text{H}_2}$  drops from a superlinear to linear regime (see Fig. 9) both contribute to the observed flattening of the  $I_{12\text{CO}}$  curve at  $N_{\text{H}_2} \simeq 10^{21} \text{ cm}^{-2}$ . However, we simultaneously observe an increase of  $T_{\text{ex}}$  above the same value of  $N_{\text{H}_2}$ . As a consequence, the curve does not completely flatten above  $N_{\text{H}_2} \simeq 10^{21} \text{ cm}^{-2}$ , as it would be expected for a highly optically thick medium, but keeps rising with a lower slope instead. Only at very high  $N_{\text{H}_2}$  values ( $\sim 10^{23} \text{ cm}^{-2}$ ),  $I_{12\text{CO}}$  becomes almost constant, as  $T_{\text{ex}}$  remains roughly constant in this regime as well. This saturation of  $T_{\text{ex}}$  with high column densities is also found in observations of Pineda, Caselli & Goodman (2008).

Considering  $I_{13\text{CO}}$  (middle panel of Fig. 10), its transition line becomes moderately optically thick at  $N_{\text{H}_2} \gtrsim 10^{22} \text{ cm}^{-2}$  due to the 69-times lower abundance of  $^{13}\text{CO}$  with respect to  $^{12}\text{CO}$ . Because of this, the change in the slope of  $I_{13\text{CO}}$  above  $N_{\text{H}_2} \simeq 10^{21} \text{ cm}^{-2}$  is more gradual than for  $I_{12\text{CO}}$  (again, the slower increase in CO abundance with  $\text{H}_2$  above  $N_{\text{H}_2} \simeq 10^{21} \text{ cm}^{-2}$  seen on Fig. 9 contributes to the change in slope). The observed increase in  $T_{\text{ex}}$  (see Fig. A3) causes also  $I_{13\text{CO}}$  to continue increasing for  $N_{\text{H}_2} > 10^{21} \text{ cm}^{-2}$ . Only at  $N_{\text{H}_2} \gtrsim 10^{23} \text{ cm}^{-2}$ ,  $I_{13\text{CO}}$  seems to level off at a roughly constant value.

The relation between  $I_{[\text{C II}]}$  and  $N_{\text{H}_2}$  for noFB runs shown in the left-hand panel of Fig. 10 closely follows the corresponding relation for the  $\text{C}^+$  column density (see Fig. 9), although also here optical depth effects can in principle influence the curve, as [C II] becomes optically thick as well at high  $N_{\text{H}_2}$  (Franeck et al. 2018). Concerning the FB runs, the larger  $I_{[\text{C II}]}$  for given  $N_{\text{H}_2}$  can be attributed to the larger fraction of excited ions due to the effects of stellar feedback, which leads to larger [C II] emission for given  $\text{C}^+$  density.

Our  $N_{\text{H}_2} - I_{[\text{C II}]}$  relation in Fig. 10 is in good agreement with real observations of the Perseus GMC by Hall et al. (2020; black squares). Remarkably, the data for the reflection nebula shown by Hall et al. (2020) exhibits a much larger  $I_{[\text{C II}]} \sim 10 \text{ K km s}^{-1}$ . This is in qualitative and quantitative agreement with our finding that our FB runs have larger  $I_{[\text{C II}]}$  values than the no-FB runs. We note that there is also a reasonable match between our data and the data of Hall et al. (2020) for the relation of  $I_{[\text{C II}]}$  and  $2 \times N_{\text{H}_2}/N_{\text{H}}$  (see Fig. A5), although observational effects can complicate the accurate determination of  $N_{\text{H}}$  as discussed in Seifried et al. (2022).

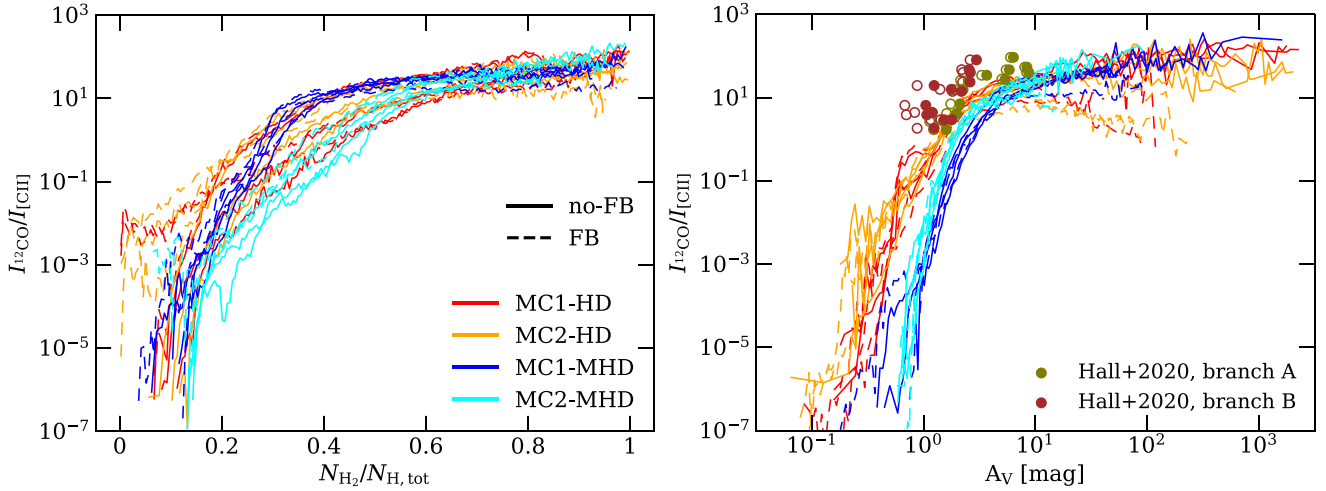


**Figure 11.** *Left:* CO/[C II] intensity ratio plotted as a function of the H<sub>2</sub> mass fraction  $N_{\text{H}_2}/N_{\text{H,tot}}$ . We plot the snapshots at different  $t_{\text{evol}}$  with the same colour. The line ratio increases with  $N_{\text{H}_2}/N_{\text{H,tot}}$ , although there is a large scatter, which is particularly relevant at high  $N_{\text{H}_2}/N_{\text{H,tot}}$  as the relation is much shallower in this regime than at lower mass fraction. This prevents the usage of  $I_{12\text{CO}}/I_{[\text{C II}]}$  to determine  $N_{\text{H}_2}/N_{\text{H,tot}}$ . *Right:* Same as in the left plot, but as a function of the visual extinction  $A_V$ . The overplotted dots represent the observational data of the Perseus Giant Molecular Cloud (GMC) from Hall et al. (2020). In particular, the empty point represent the original data, and the filled points represent the data with the  $A_V$  that would be required to obtain the same effective ISRF, if the unshielded ISRF in the Perseus GMC was the same as in the solar neighbourhood (see equation 25). The two branches correspond to different regions of that cloud. The larger  $I_{12\text{CO}}/I_{[\text{C II}]}$ , for given  $A_V$  in Perseus GMC is likely due to the lower ISRF in Perseus GMC than in the solar neighbourhood.

In Fig. 4 we have already shown that the [C II] luminosity is enhanced by stellar feedback. Next, we analyse the column density regimes where the majority of luminosity comes from. For  $N_{\text{H}_2} \geq 10^{22} \text{ cm}^{-2}$  we report typical  $I_{[\text{C II}]}$  values of 1–10 K km s<sup>-1</sup> for noFB runs and up to a few  $\sim 10^2$  K km s<sup>-1</sup> for feedback runs (right-hand panel of Fig. 10). Stellar feedback increases the [C II] excitation temperature, which causes a stronger emission for a given density. In general, areas with the highest  $N_{\text{C}^+}$  are those closer to the star-forming regions (see Fig. 1). Therefore, this is also the regime where the difference between FB and noFB runs are most evident. In addition, for the HD clouds (red and orange lines) at late evolutionary stages, stellar feedback affects even larger parts of the clouds, such that the enhancement in  $I_{[\text{C II}]}$  is visible also in lower column density regimes.

#### 4.6.2 $I_{\text{CO}}/I_{[\text{C II}]}$ and H<sub>2</sub> mass fraction

In Section 4.5 we show that there is no clear relation between the CO/[C II] luminosity ratio and the H<sub>2</sub> mass fraction. Now, we consider the intensity ratio  $I_{12\text{CO}}/I_{[\text{C II}]}$  as a function of the column density ratio  $N_{\text{H}_2}/N_{\text{H,tot}}$  and of the visual extinction  $A_V$ , defined as

$$A_V = (N_{\text{H,tot}} \times 5.348 \times 10^{-22} \text{ cm}^{-2}) \text{ mag} , \quad (21)$$

in agreement with Draine & Bertoldi (1996), for each pixel of the maps. We need to be sure that we consider the same portion of the cloud for both, CO and C<sup>+</sup>. For this purpose, we loop over the 201 velocity channels of the maps and indicate with  $\{k\}$  the set of channels for which both specific intensities,  $I_{v,k,12\text{CO}}$  and  $I_{v,k,[\text{C II}]}$ , are above the specific intensity of the CMB, corresponding to antenna temperatures of 0.84 and  $2.69 \times 10^{-13}$  K for <sup>12</sup>CO and [C II], respectively. These values are obtained by using the antenna temperature definition (equation 15) at the CO and [C II] line frequencies for the CMB intensity. We define

$$I_{12\text{CO}} = \sum_k I_{v,k,12\text{CO}} \Delta v , \quad (22)$$

where  $\Delta v$  is the width of a velocity channel,  $I_{[\text{C II}]}$  is obtained analogously. The result is shown in Fig. 11, where the mean values of the distribution of  $I_{\text{CO}}/I_{[\text{C II}]}$  for a given  $N_{\text{H}_2}$  (left) and for a given  $A_V$  (right) are represented using again the same colour for snapshots referring to different  $t_{\text{evol}}$ . We show here the data referring to the LOS along the  $z$ -axis, but we obtain analogous results for the integration along the other LOS. The  $I_{12\text{CO}}/I_{[\text{C II}]}$  ratio increases with increasing  $N_{\text{H}_2}/N_{\text{H,tot}}$ . However, different clouds and snapshots show significantly different line ratios for given  $N_{\text{H}_2}/N_{\text{H,tot}}$  with a typical scatter of up to two orders of magnitude. At very low values of  $N_{\text{H}_2}/N_{\text{H,tot}}$  the scatter is even larger due to the low statistics. Furthermore, the presence of CO-dark and CO-bright pixels for the same  $N_{\text{H}_2}$  (as shown in detail in Seifried et al. 2020a, see their fig. 8) also contributes to enlarge such scatter.

The relation between  $I_{12\text{CO}}/I_{[\text{C II}]}$  and  $A_V$  (right plot of Fig. 11) exhibits a qualitatively similar trend to the relation with  $N_{\text{H}_2}/N_{\text{H,tot}}$ . However, in this case a modest split between HD and MHD clouds is recognizable at low  $A_V$ , and between no-FB and FB clouds is recognizable at high  $A_V$ . We overplot real observational data of the Perseus GMC from Hall et al. (2020). The Perseus GMC  $I_{12\text{CO}}/I_{[\text{C II}]}$  values, for given  $A_V$ , are larger than in our simulations. We comment on this in Section 5.1.

In conclusion, the variability for a given  $N_{\text{H}_2}/N_{\text{H,tot}}$  value is so large that the ratio  $I_{12\text{CO}}/I_{[\text{C II}]}$  cannot be reliably used to determine  $N_{\text{H}_2}/N_{\text{H,tot}}$ . This is also shown in the example given in Fig. 12, where we show a map of  $I_{12\text{CO}}/I_{[\text{C II}]}$  for MC1-HD-noFB at  $t_{\text{evol}} = 4$  Myr. We overplot isocontour lines corresponding to H<sub>2</sub> mass fractions of 0.1, 0.3, 0.5, 0.7, and 0.9. There is a general correspondence between high line ratios and high H<sub>2</sub> mass fractions, but there are still significant variations in the line ratio within regions of similar H<sub>2</sub> mass fraction, especially for mass fraction regimes between 0.3 and 0.7.

Our results for the *pixel-by-pixel* approach are thus similar to that for the global luminosity ratio shown in Fig. 8, which also does not allow for a determination of the global H<sub>2</sub> mass fraction. However, we cannot directly compare the relation between  $I_{12\text{CO}}/I_{[\text{C II}]}$  and

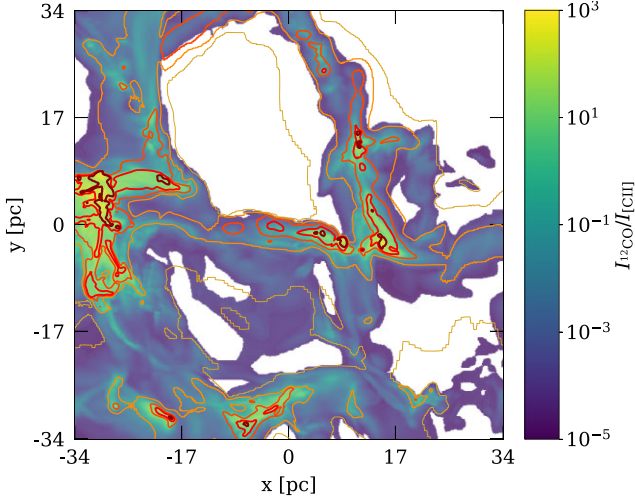


**Figure 12.** Map of  $I_{12\text{CO}}/I_{[\text{C II}]}$  for MC1-HD at  $t_{\text{evol}} = 4$  Myr. Contour lines indicate an  $\text{H}_2$  mass fraction  $N_{\text{H}_2}/N_{\text{H,tot}}$  of 0.1, 0.3, 0.5, 0.7, and 0.9, respectively. We note a general correspondence between higher intensity ratio and higher  $N_{\text{H}_2}/N_{\text{H,tot}}$  values. There are, however, significant differences in the line ratio for a given  $N_{\text{H}_2}/N_{\text{H,tot}}$  value, especially in moderate  $N_{\text{H}_2}/N_{\text{H,tot}}$  regimes.

$N_{\text{H}_2}/N_{\text{H,tot}}$  with the one between  $L_{12\text{CO}}/L_{[\text{C II}]}$  and  $M_{\text{H}_2}/M_{\text{H,tot}}$ . For the pixel-by-pixel approach we also find  $\text{H}_2$  column density fractions close to 0 and 1 and corresponding  $I_{12\text{CO}}/I_{[\text{C II}]}$  values spanning eight orders of magnitude. On the other hand, when analysing  $L_{12\text{CO}}/L_{[\text{C II}]}$ , we average over the entire cloud and, as a consequence, both the mass fraction and the luminosity ratio span over a considerably lower range.

## 5 DISCUSSION

### 5.1 Intrinsic variability of line ratios

The  $^{12}\text{CO}/[\text{C II}]$  and  $^{13}\text{CO}/[\text{C II}]$  line ratios shown in Fig. 8 are characterized by a large dispersion due to the difference in the structure and evolutionary stage of the clouds themselves only, but not to different environments or external factors. In fact, all clouds form in a portion of a galactic disc with the same CRIR,  $G_0$ , and metallicity and with turbulence driven by supernovae. Furthermore, all MHD runs have the same initial magnetic field strength. Despite that,  $L_{12\text{CO}}/L_{[\text{C II}]}$  varies by up to a factor of 5 for a given  $M_{\text{H}_2}/M_{\text{H,tot}}$ . The same applies for  $^{13}\text{CO}$ , although the scatter among different LOS for the same snapshot is reduced because of the reduced optical depth.

This scatter is also found in other works. For instance, Röellig et al. (2006) use the luminosity ratio to assess the environmental conditions like the cloud metallicity, density, and far-ultraviolet (FUV) field intensity.<sup>4</sup> Their models also exhibit large difference in the line ratio up to a factor of a few, even when leaving environmental conditions like the metallicity, FUV, and cloud density unchanged. Furthermore, also observational results at similar metallicities quoted in their work e.g. for the LMC and 30 Doradus, show a similar scatter of 5–10 in the  $[\text{C II}]/^{12}\text{CO}$  line ratio. In summary, as already stated by Röellig et al.

<sup>4</sup>In order to compare values from observational works with our simulations, it might be necessary to convert the intensity from  $\text{K km s}^{-1}$  to  $\text{erg s}^{-1} \text{cm}^{-2}$  and recalculate the luminosity and luminosity ratio (see Fig. A4). Note that we plot  $[\text{C II}]/\text{CO}$  there, whereas Fig. 8 shows  $\text{CO}/[\text{C II}]$ .

(2006), we do not recommend to use  $L_{12\text{CO}}/L_{[\text{C II}]}$  to infer physical properties of the clouds.

Furthermore, Madden et al. (2020) analyse the  $^{12}\text{CO}$  and  $[\text{C II}]$  emission in a variety of environments. For normal galaxies and galactic star-forming regions, they find  $L_{[\text{C II}]} / L_{12\text{CO}} \approx 4000$ , with a large scatter covering values from 300 to 25 000. Our simulation results are thus in good agreement with their findings, although they consider a much larger variety of environments.

As we already mentioned, Hall et al. (2020) analysed the  $^{12}\text{CO}$  ( $1 \rightarrow 0$ ) and  $[\text{C II}]$  emission from two regions of the Perseus GMC. As their observations refer to a resolved portion of a cloud, this corresponds to our *pixel-by-pixel* analysis shown in Fig. 11. Their observational data are overplotted with empty circles in the right plot of the figure. In general, we find that their reported values of  $I_{12\text{CO}}/I_{[\text{C II}]}$  of 2–100 agree well with ours. However, for given  $I_{12\text{CO}}/I_{[\text{C II}]}$ , the  $A_V$  values of Hall et al. (2020) are smaller by a factor of  $\sim 2$  with respect to the values of our simulations. This can in parts be due to the lower ISRF in the Perseus GMC which is only about  $\sim 0.4$ -times the ISRF in solar neighbourhood i.e. that used here (Lee et al. 2014). We can relate the visual extinction between both cases in the following way:

$$\text{ISRF}_P = \text{ISRF}_{P,0} \times e^{-\gamma A_{V,P}} \quad (23)$$

$$\text{ISRF}_{P,0} = \text{ISRF}_{\text{sol}} \times 0.4 = \text{ISRF}_{\text{sol}} \times e^{-\gamma A_{V,\text{ref}}} \quad (24)$$

Here,  $\text{ISRF}_{P,0}$  is the unattenuated ISRF in Perseus i.e. 0.4-times the solar neighbourhood value,  $\text{ISRF}_{\text{sol}}$ . Furthermore,  $A_{V,P}$  is the visual extinction given by Hall et al. (2020) and  $A_{V,\text{ref}}$  is the correction to translate their visual extinction to ours. We use a value of  $\gamma = 2.5$  typical for dust extinction in the ultraviolet range. From that it follows that the value of the visual extinction given by the authors translates in our reference frame to

$$A_V = A_{V,P} + A_{V,\text{ref}} = A_{V,P} - \frac{\ln(0.4)}{\gamma} = A_{V,P} + 0.367. \quad (25)$$

This means that the  $A_V$  at which the strength of the ISRF in Perseus is identical to that in the solar neighbourhood is about 0.367 mag lower than in our reference frame. In order to take this into account, in Fig. 11 we plot – beside the empty circles showing the original data from Hall et al. (2020) – with filled circles their data, but with an  $A_V$  increased by 0.367 mag (i.e. the  $A_V$  in the reference ISRF used in our simulations). This enables a more direct comparison with our data. Indeed, in this way the observed points are now in better agreement though still shifted slightly towards the left. One reason for this difference could be due to the fact that the definition of  $A_V$  used in Hall et al. (2020) is different from ours, as it is based on dust optical depth and starlight reddening along the LOS. This can also lead to slightly different values.

Finally, Bisbas et al. (2021) analysed the line emission of several species from two different, simulated clouds with different environmental parameters. For comparable CRIR,  $G_0$ , and metallicity, they find  $^{12}\text{CO}/[\text{C II}]$  line ratios larger by up to one order of magnitude compared to our work. We tentatively attribute this difference to two main factors. First, our clouds are somewhat more diffuse than the clouds used by Bisbas et al. (private communication). Indeed, when going to later evolutionary states i.e. denser clouds, our line ratios increase (Fig. 8). Secondly, their work assumes chemical equilibrium, while we use non-equilibrium chemistry, a difference whose effects we will discuss in detail in the following.

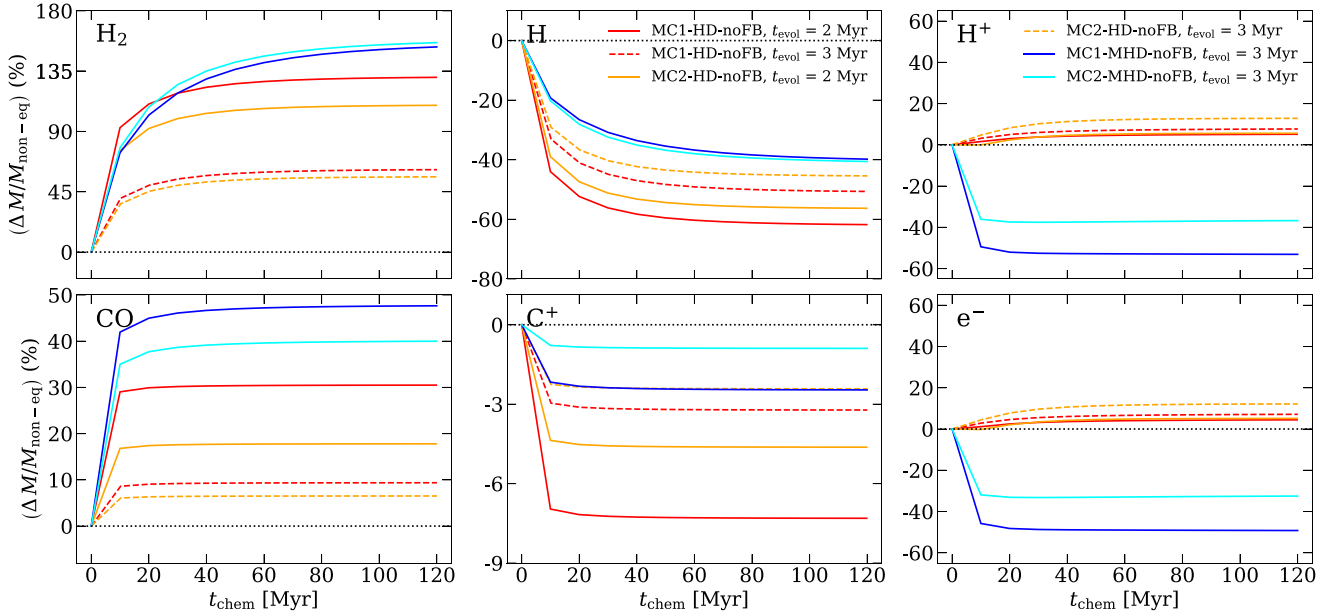


**Figure 13.** Relative mass changes of  $\text{H}_2$ ,  $\text{H}$ ,  $\text{H}^+$ ,  $\text{CO}$ ,  $\text{C}^+$ , and  $\text{e}^-$  (from top left to bottom right) for a selection of snapshots, obtained by freezing the evolution of the physics in the simulation and only evolving the chemistry for a time  $t_{\text{chem}}$ .  $\text{CO}$  and  $\text{C}^+$  reach equilibrium after  $\sim 10$  Myr, whereas  $\text{H}$  and  $\text{H}_2$  reach equilibrium at  $\gtrsim 40$  Myr. The mass variations at equilibrium are particularly important for  $\text{H}$  (decreasing by up to 60 per cent) and for  $\text{H}_2$  (increasing by up to 160 per cent), making the assumption of equilibrium for these species questionable. Changes for carbon-bearing species,  $\text{H}^+$ , and  $\text{e}^-$  are smaller than for  $\text{H}$  and  $\text{H}_2$ .

## 5.2 Equilibrium versus non-equilibrium chemistry

A large number of MC simulation works post-process their results to obtain chemical abundances by assuming that the chemical state is in equilibrium (see e.g. Gong et al. 2018; Li et al. 2018; Keating et al. 2020; Bisbas et al. 2021). As an example, Gong et al. (2020) study the  $X_{\text{CO}}$  factor for a wide range of environments. They evolve the chemical network for 50 Myr i.e. equilibrium is roughly reached at that point (Joshi et al. 2019), before analysing synthetic  $\text{CO}$  observations and the  $X_{\text{CO}}$  factor. However, the presence of phenomena like e.g. the turbulent mixing (see e.g. Valdivia et al. 2016; Glover & Mac Low; Seifried et al. 2017) suggests that this approach can determine inaccurate estimations at least for hydrogen and directly related quantities like e.g.  $X_{\text{CO}}$ .

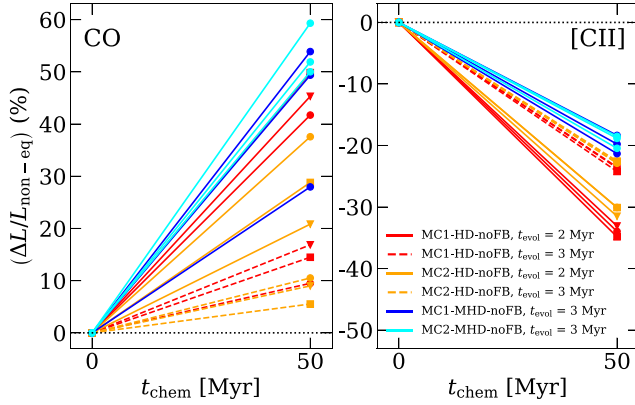
Here, we aim to assess how much the assumption of equilibrium chemistry affects synthetic emission maps. In order to do so, we first select the snapshots of MC1-HD-noFB and MC2-HD-noFB at  $t_{\text{evol}} = 2$  and 3 Myr, as well as of MC1-MHD-noFB and MC2-MHD-noFB at  $t_{\text{evol}} = 3$  Myr, and only evolve the chemistry with the NL97 network for additional 120 Myr while the hydrodynamical state (total gas density, etc.) remains frozen. In the following,  $t_{\text{chem}}$  refers to the time for which the chemistry of the snapshot was evolved. We also define  $M_{\text{no-eq}} = M(t_{\text{chem}} = 0)$  and  $L_{\text{no-eq}} = L(t_{\text{chem}} = 0)$ .

Fig. 13 shows the evolution of  $\text{H}_2$ ,  $\text{H}$ ,  $\text{H}^+$ ,  $\text{CO}$ ,  $\text{C}^+$ , and  $\text{e}^-$  as a function of  $t_{\text{chem}}$ . The  $\text{CO}$  and  $\text{H}_2$  masses (left column) increase with  $t_{\text{chem}}$  by up to 50 and 160 per cent, respectively, in rough agreement with e.g. Gong et al. (2018). The masses of  $\text{H}^+$  and  $\text{e}^-$  have a different behavior for HD and MHD clouds. We attribute this difference to a different behaviour in the density regime from  $10^{-26}$  to  $10^{-23}$   $\text{g cm}^{-3}$ : here, the vast majority of the cells in MHD runs is associated with a decrease in the abundance of  $\text{H}^+$  as we approach equilibrium, whereas in the HD runs, a much larger fraction is associated with an increase of  $\text{H}^+$ . This could be related to different histories already before we start to zoom in on the individual clouds in the 3D, SILCC-Zoom simulations. This could then lead to a

different evolution of  $\text{H}^+$  with  $t_{\text{chem}}$  as dictated by the interplay of cosmic ray ionization and recombination. In contrast, in high-density regions, for both the HD and MHD case the abundance of  $\text{H}^+$  strongly decreases for the equilibrium case (as expected, due to recombination dominating) and thus cannot contribute the different behaviour. However, as the total mass fraction of  $\text{H}^+$  of the clouds is only of the order of 0.1 per cent, and thus not particularly relevant for neither the dynamics nor the emission maps, we do not follow this up further here. In summary, these results once again confirm that the assumption of chemical equilibrium is – in particular for hydrogen-bearing species – questionable (Glover & Mac Low; Valdivia et al. 2016; Seifried et al. 2017, 2022; Hu et al. 2021).

Furthermore, we find that  $\text{CO}$  and  $\text{C}^+$  reach equilibrium at  $t_{\text{chem}} \sim 10$  Myr, whereas  $\text{H}_2$ ,  $\text{H}$ , and  $\text{H}^+$  reach it after  $\gtrsim 40$  Myr for the HD clouds, and after  $\gtrsim 80$  Myr for the MHD clouds, which are less dense, and therefore further from equilibrium. In all cases, however, we can assume that at  $t_{\text{chem}} = 50$  Myr (used in the following) equilibrium is roughly reached, as the relative changes with respect to later times are  $\lesssim 10$  per cent.

The significant changes of the chemical abundances by up to 160 per cent also affect the synthetic emission maps. In Fig. 14 we show the difference in total luminosity between the equilibrium (defined here as the state at  $t_{\text{chem}} = 50$  Myr) and non-equilibrium state ( $t_{\text{chem}} = 0$ ) for  $^{12}\text{CO}$  and  $[\text{C II}]$ . The luminosity of  $\text{CO}$  increases in equilibrium by up to 60 per cent with respect to the non-equilibrium case. This increase is only marginally larger than the respective increase of the  $\text{CO}$  mass (up to 50 per cent), indicating that the increase in  $M_{\text{CO}}$  in chemical equilibrium is responsible for this luminosity change. Furthermore, due to the different gain in  $M_{\text{H}_2}$  (top left-hand panel of Fig. 13) and  $L_{\text{CO}}$ , the value of  $X_{\text{CO}}$  determined for the chemical equilibrium case is about 50 per cent larger than the actual value for the non-equilibrium state. However, this deviation is within the typical scatter of  $X_{\text{CO}}$  of a factor of a few found here (see Section 4.4) as well as in Gong et al. (2020) using equilibrium chemistry. Hence, differences caused by the equilibrium approach



**Figure 14.** Relative luminosity changes of  $L_{\text{CO}}$  (left) and  $L_{[\text{CII}]}$  (right) between  $t_{\text{chem}} = 0$  and  $t_{\text{chem}} = 50$  Myr for the same selection of snapshots as in Fig. 13. The three different LOS are indicated with different markers. We note that the the luminosity decreases for [C II] up to  $\sim 30$  per cent, while the corresponding mass decreases of  $\sim 7$  per cent. The changes in the CO luminosity are comparable with the changes in the CO mass.

can hardly be assessed by comparing the values for  $X_{\text{CO}}$  obtained in both works.

On the other hand, the change in [C II] luminosity (right-hand panel of Fig. 14) is considerably larger than the corresponding change in mass (as shown in Fig. 13) e.g. for MC1-HD-noFB at 2 Myr for one LOS we have  $\Delta L/L_{\text{non-eq}} \simeq -30$  per cent and  $\Delta M/M_{\text{non-eq}} \simeq -7$  per cent.

One element contributing to explain the changes in mass and luminosity are the collisional partners, which in our case are  $\text{H}_2$ , H, and electrons. We find that the  $\text{H}_2$  abundance increases with  $t_{\text{chem}}$ , whereas H decreases. Although the electron abundance increases for the equilibrium case and the  $\text{C}^+e^-$  de-excitation rates are in general larger than those of H and  $\text{H}_2$ , this does not lead to an increase in  $L_{[\text{CII}]}$ . We attribute this to the fact that the relative change of the electron abundance is significantly lower ( $\lesssim 12$  per cent) than for the other two collisional partners. Additionally, there is little  $\text{C}^+$  in the low-density/high-temperature regime where the  $e^-$  collisional rate is high. Hence, as the [C II] emission is dominated by atomic gas (Franeck et al. 2018), the drop in H mass is mainly responsible for the drop in  $L_{[\text{CII}]}$ .

The impact of the collisional partners affecting  $L_{[\text{CII}]}$  can also be expressed by the excitation temperature (see Fig. A6 in Appendix A). We find that  $T_{\text{ex}}$  is overall lower for the equilibrium case. This contributes to explain the larger decrease in luminosity than in mass when moving to equilibrium for  $\text{C}^+$ .

Another factor explaining why the relative changes of mass and luminosity for  $\text{C}^+$  do not directly correlate is connected to the detailed distribution of  $\text{C}^+$  in the density – temperature phase space. The majority of  $\text{C}^+$  mass is contained in the Warm Neutral Medium (WNM) i.e. the portion of the ISM where hydrogen is mainly in atomic form, with temperature  $\sim 8000$  K, where the  $\text{C}^+$  abundance is already quite close to chemical equilibrium. Thus, evolving the chemistry to equilibrium does not imply a major change in this region and then the overall change in  $M_{\text{C}^+}$  is rather moderate. However, for observations towards MCs, the  $\text{C}^+$  in the WNM – despite existing in this environment – contributes only little to the total [C II] luminosity. Rather, most of the [C II] luminosity from MCs comes from the Cold Neutral Medium (CNM) i.e. those regions with mostly atomic hydrogen and temperature  $\sim 100$  K (Franeck et al. 2018). In the CNM, however, the  $\text{C}^+$  abundance is further away from equilibrium,

hence evolving the chemistry to equilibrium produces a significant change in the  $\text{C}^+$  mass in this region, and in consequence on the total [C II] luminosity. The total change in  $\text{C}^+$  mass (being dominated by the WNM) is, however, minor.

We emphasize that the values for  $t_{\text{evol}} = 2$  Myr (solid lines in Figs 13 and 14) change more, both in terms of mass and luminosity, than the values for  $t_{\text{evol}} = 3$  Myr (dashed lines). Hence, early evolutionary stages appear to be further away from a chemical equilibrium state, as the overall densities are still lower and thus, the chemical time-scales longer. This phenomenon is confirmed by the MHD clouds, which, as we already discussed (Section 4.1), evolve more slowly than the HD clouds. Therefore, the MHD clouds at  $t_{\text{evol}} = 3$  Myr are at a relatively early evolutionary stage. Hence, due to the corresponding lower density contrast and less pronounced density peaks (see Section 4.1), the chemical time scales are longer i.e. overall the MHD clouds are further from equilibrium than the HD clouds. In particular, the larger increase in the  $\text{H}_2$  mass for the MHD clouds is associated with a lower decrease of H. We note that  $\text{H}^+$  is subdominant in terms of mass at any time compared to H and  $\text{H}_2$ . Hence, the opposite trend for  $\text{H}^+$  is mainly caused by the evolution of  $\text{H}_2$  and H and the constraint given by the total hydrogen mass (i.e.  $m_{\text{H}^+} = m_{\text{Htot}} - m_{\text{H}_2} - m_{\text{H}}$ ). Furthermore, as the majority of electrons is provided by  $\text{H}^+$ , also the electron mass evolution shows an opposite trend for the MHD clouds. As a result, we argue that the chemical post-processing of MC simulations up to equilibrium, in particular at an early evolutionary state, is questionable and should be considered with great caution.

Given the luminosity changes shown in Fig. 14, the values of  $L_{\text{CO}}/L_{[\text{CII}]}$  (not shown) increase by up to 100 per cent for the equilibrium case with respect to the non-equilibrium case. Assuming chemical equilibrium can therefore lead to a relative error of up to a factor of  $\sim 2$  when calculating such line ratios. As pointed out before, this error is generally larger at early evolutionary stages of the clouds. This effect can thus contribute to the differences seen in line ratios when compared to e.g. the work of Bisbas et al. (2021).

Next, we investigate the change in the relation between  $N_{\text{H}_2}$  and  $N_{\text{CO}}$  assuming chemical equilibrium. In Fig. 15 we show an example for MC2-HD-noFB at  $t_{\text{evol}} = 2$  Myr. The red-shaded area represents the 2D-PDF for the original, non-equilibrium snapshot, whereas the blue-shaded area represents the equilibrium case. The two lines indicate the mean values. We observe a shift towards higher  $N_{\text{H}_2}$  for a given  $N_{\text{CO}}$  for chemical equilibrium, which we mainly attribute to the more pronounced increase in  $M_{\text{H}_2}$  than in  $M_{\text{CO}}$  in case of chemical equilibrium (see Fig. 13). We note that this is in excellent agreement with results of Hu et al. (2021), who find a similar difference in mass changes for  $\text{H}_2$  and CO concerning equilibrium and non-equilibrium states.

Finally, we note that we did not consider FB runs in this equilibrium versus non-equilibrium analysis. This is due to the fact that the post-processing of the feedback-affected regions with CLOUDY, described in Section 3.2, is based on the assumption of chemical equilibrium in those regions. Furthermore, in the regions not affected by stellar feedback, the chemical evolution is acting in an identical matter as for the noFB runs, which is why we refrain from showing these results here.

To summarize, we consider it as crucial to use non-equilibrium chemistry to simulate the  $\text{H}/\text{H}_2$  content of MCs, as cloud evolution and molecule formation go hand in hand. Because of this, using chemical equilibrium for simulated MCs should be considered with great caution, in particular at early evolutionary stages, as it can significantly effect both the masses and luminosities of the various species.

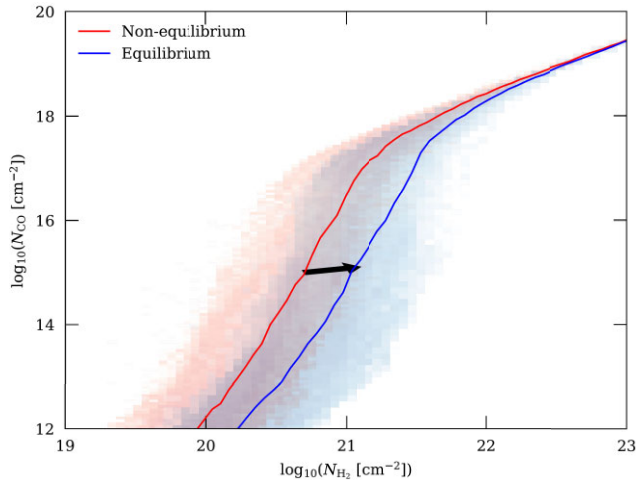


**Figure 15.**  $N_{\text{CO}}$  as a function of  $N_{\text{H}_2}$  for MC2-HD at  $t_{\text{evol}} = 2$  Myr, considering the chemical state in non-equilibrium (red) and at equilibrium (blue). Shaded areas represent the 2D-PDFs and solid lines represent the mean values. The change is due to the larger increase in the  $\text{H}_2$  mass than in the CO mass when moving from non-equilibrium to equilibrium chemistry (120 per cent versus 30 per cent for the considered snapshot). The black arrow qualitatively indicates the change of the abundances for this transition.

## 6 CONCLUSIONS

We present an analysis of the abundance and luminosity of  $^{12}\text{CO}$ ,  $^{13}\text{CO}$ , and  $\text{C}^+$  for eight simulated MCs within the SILCC-Zoom project (Seifried et al. 2017), in which the chemical network is evolved *on-the-fly*. In particular, we investigate two clouds with and two without magnetic fields under solar neighbourhood conditions at different evolutionary stages. For each simulation we consider a reference case without stellar feedback and one including radiative feedback in the form of ionizing radiation by massive stars. For this purpose, we have developed a novel post-processing routine (based on CLOUDY) to account for higher ionization states of carbon. We show that this post-processing is essential to obtain reliable [C II] emission maps in feedback-dominated regions.

Our conclusions can be summarized as follows:

(i) The [C II] emission maps of the runs with radiative feedback show expanding H II regions/bubbles, where carbon is largely in form of  $\text{C}^{2+}$  and thus devoid of [C II] emission inside, but with significant emission at the rims. This is in good agreement with recent [C II] surveys.

(ii) We estimate that radiative feedback increases the [C II] luminosity by  $\sim 50$ – $85$  per cent compared to the non-feedback case due to an enhancement of the excitation temperature. The CO luminosity decreases by up to a factor of 3 at late evolutionary stages of the clouds due to the dispersal of dense regions.

(iii) The line luminosity ratios  $L_{12\text{CO}}/L_{[\text{C II}]}$  and  $L_{13\text{CO}}/L_{[\text{C II}]}$ , integrated over the entire maps, show an increase with increasing  $\text{H}_2$  mass fraction in noFB runs, but no clear relation in FB runs. We obtain values for  $L_{12\text{CO}}/L_{[\text{C II}]}$  from 1 to 6 and for  $L_{13\text{CO}}/L_{[\text{C II}]}$  from 0.1 to 1.1. We argue that due to the large spread, these line ratios *cannot* be used as a reliable tracer of the cloud’s  $\text{H}_2$  mass fraction. Similarly, this spread makes it difficult to use them to assess environmental parameters like the CRIR, the IRSF, or the metallicity, which we kept fixed in our simulations.

(iv) A pixel-by-pixel analysis of  $I_{12\text{CO}}/I_{[\text{C II}]}$  as a function of  $N_{\text{H}_2}/N_{\text{H,tot}}$  shows an increase of the ratio with  $N_{\text{H}_2}/N_{\text{H,tot}}$ . However,

as for the total luminosity ratio, also here the scatter is so significant that  $I_{12\text{CO}}/I_{[\text{C II}]}$  cannot reliably be used to predict the mass fraction of  $\text{H}_2$  along the LOS.

(v) Evolving the chemistry to equilibrium as done in various works results in significant differences in terms of species abundance with respect to a self-consistent non-equilibrium approach used *on-the-fly* during the simulation. Hence, in particular for early evolutionary stages an equilibrium approach is questionable. We find that for the equilibrium case, the  $\text{H}_2$  mass is increased and the H mass is decreased by up to a factor of about 2. Other species abundances such as CO,  $\text{C}^+$ , and electrons change by a few 10 per cent.

(vi) Assuming chemical equilibrium also affects the inferred luminosities of CO and [C II], with relative changes of up to +50 and  $-30$  per cent, respectively. These luminosity changes cause an overestimate of the  $L_{\text{CO}}/L_{[\text{C II}]}$  line ratios by up to 100 per cent if equilibrium chemistry is assumed. Similarly, the  $X_{\text{CO}}$  factor would be overestimated by up to 50 per cent in this case.

(vii) In general, the  $X_{\text{CO}}$  factor ranges between  $0.5$  and  $4.5 \times 10^{20} \text{ cm}^{-2} \text{ K}^{-1} \text{ km}^{-1} \text{ s}$ , showing no clear trend with respect to time evolution or the  $\text{H}_2$  mass fraction. Feedback runs in general have a lower  $X_{\text{CO}}$  than the corresponding non-feedback runs. The similarly defined  $X_{[\text{C II}]}$  factor ranges between  $0.5$  and  $12 \times 10^{20} \text{ cm}^{-2} \text{ K}^{-1} \text{ km}^{-1} \text{ s}$ , also not showing a clear trend with evolutionary time or  $\text{H}_2$  mass fraction.

In summary, we show that it is crucial to take into account the effects (i) of stellar radiation in further ionizing  $\text{C}^+$  within H II regions, and (ii) an *on-the-fly*, non-equilibrium chemistry treatment to accurately model CO and [C II] line emission in simulated MCs. We thus strongly suggest to consider both effects for future and more detailed comparisons with observations (e.g. Ebagezio et al., in preparation).

## ACKNOWLEDGEMENTS

The authors thank the anonymous referee for the constructive and helpful comments which contributed to improve the clarity of the paper. The authors also thank KP Hall for providing the observational data used in some of the figures. SW and PCN gratefully acknowledge the European Research Council under the European Community’s Framework Programme FP8 via the ERC Starting Grant RADFEEDBACK (project number 679852). SE, DS, SW, TER, and PCN further thank the Deutsche Forschungsgemeinschaft (DFG) for funding through the SFB 956 ‘The conditions and impact of star formation’ (sub-projects C5 and C6). Furthermore, the project is receiving funding from the programme ‘Profilbildung 2020’, an initiative of the Ministry of Culture and Science of the State of Northrhine Westphalia. The sole responsibility for the content of this publication lies with the authors. TN acknowledges support from the DFG under Germany’s Excellence Strategy – EXC-2094 - 390783311 from the DFG Cluster of Excellence ‘ORIGINS’. The software used in this work was in part developed by the DOE NNSA-ASC OASCR Flash Center at the University of Chicago. We particularly thank the Regional Computing Center Cologne for providing the computational facilities for this project by hosting our supercomputing cluster ‘Odin’.

## DATA AVAILABILITY

The data underlying this article will be shared on reasonable request to the corresponding author.

## REFERENCES

- Abel N. P., Ferland G. J., Shaw G., van Hoof P. A. M., 2005, *ApJS*, 161, 65
- Appleton P. N. et al., 2013, *ApJ*, 777, 66
- Arzoumanian D., André P., Peretto N., Könyves V., 2013, *A&A*, 553, A119
- Beck R., Wielebinski R., 2013, in Oswalt T. D., Gilmore G., eds, *Planets, Stars and Stellar Systems. Volume 5: Galactic Structure and Stellar Populations*, Vol. 5, Springer Science + Business Media, Dordrecht (NL), p. 641
- Beuther H. et al., 2014, *A&A*, 571, A53
- Bisbas T. G., Tan J. C., Tanaka K. E. I., 2021, *MNRAS*, 502, 2701
- Bolatto A. D., Wolfire M., Leroy A. K., 2013, *ARAA*, 51, 207
- Borchert E. M. A., Walch S., Seifried D., Clarke S. D., Franck A., Nürnberger P. C., 2022, *MNRAS*, 510, 753
- Bot C., Boulanger F., Rubio M., Rantakyro F., 2007, *A&A*, 471, 103
- Bouchut F., Klingenberg C., Waagan K., 2007, *Numer. Math.*, 108, 7
- Cecchi-Pestellini C., Bodo E., Balakrishnan N., Dalgarno A., 2002, *ApJ*, 571, 1015
- Chabrier G., 2001, *ApJ*, 554, 1274
- Clark P. C., Glover S. C. O., Klessen R. S., Bonnell I. A., 2012, *MNRAS*, 424, 2599
- Dame T. M., Koper E., Israel F. P., Thaddeus P., 1993, *ApJ*, 418, 730
- Dame T. M., Hartmann D., Thaddeus P., 2001, *ApJ*, 547, 792
- Derigs D., Winters A. R., Gassner G. J., Walch S., 2016, *J. Comput. Phys.*, 317, 223
- Derigs D., Winters A. R., Gassner G. J., Walch S., Böhm M., 2018, *J. Comput. Phys.*, 364, 420
- Dobbs C. L., Pringle J. E., 2013, *MNRAS*, 432, 653
- Dobbs C. L. et al., 2014, *Protostars and Planets VI*, University of Arizona Press, Tucson, p.3
- Draine B. T., 1978, *ApJS*, 36, 595
- Draine B. T., Bertoldi F., 1996, *ApJ*, 468, 269
- Dubey A., Reid L. B., Fisher R., 2008, *Phys. Scr.*, 132
- Dullemond C. P., Juhasz A., Pohl A., Sereshti F., Shetty R., Peters T., Commercon B., Flock M., 2012, *Astrophysics Source Code Library*, record ascl:1202.015
- Federrath C., Banerjee R., Clark P. C., Klessen R. S., 2010, *ApJ*, 713, 269
- Ferland G. J. et al., 2017, *Rev. Mex. Astron. Astrofis.*, 53, 385
- Franck A. et al., 2018, *MNRAS*, 481, 2477
- Fryxell B. et al., 2000, *ApJS*, 131, 273
- Ganguly S., Walch S., Clarke S. D., Seifried D., 2022, preprint (arXiv:2204.02511)
- Gatto A. et al., 2015, *MNRAS*, 449, 1057
- Gatto A. et al., 2017, *MNRAS*, 466, 1903
- Gerlich D., 1990, *J. Chem. Phys.*, 92, 2377
- Girichidis P. et al., 2016, *MNRAS*, 456, 3432
- Girichidis P., Seifried D., Naab T., Peters T., Walch S., Wünsch R., Glover S. C. O., Klessen R. S., 2018, *MNRAS*, 480, 3511
- Glover S. C. O., Clark P. C., 2016, *MNRAS*, 456, 3596
- Glover S. C. O., Mac Low M.-M., 2007a, *ApJS*, 169, 239
- Glover S. C. O., Mac Low M.-M., 2007b, *ApJ*, 659, 1317
- Glover S. C. O., Mac Low M. M., 2011, *MNRAS*, 412, 337
- Glover S. C. O., Federrath C., Mac Low M. M., Klessen R. S., 2010, *MNRAS*, 404, 2
- Gong M., Ostriker E. C., Kim C.-G., 2018, *ApJ*, 858, 16
- Gong M., Ostriker E. C., Kim C.-G., Kim J.-G., 2020, *ApJ*, 903, 142
- Grenier I. A., Casandjian J.-M., Terrier R., 2005, *Science*, 307, 1292
- Habing H. J., 1968, *Bull. Astron. Inst. Netherlands*, 19, 421
- Haid S., Walch S., Seifried D., Wünsch R., Dinbier F., Naab T., 2019, *MNRAS*, 482, 4062
- Hall K. P., Stanimirović S., Lee M.-Y., Wolfire M., Goldsmith P., 2020, *ApJ*, 899, 23
- Hu C.-Y., Naab T., Walch S., Glover S. C. O., Clark P. C., 2016, *MNRAS*, 458, 3528
- Hu C.-Y., Naab T., Glover S. C. O., Walch S., Clark P. C., 2017, *MNRAS*, 471, 2151
- Hu C.-Y., Sternberg A., van Dishoeck E. F., 2021, *ApJ*, 920, 44
- Hu C.-Y., Schrubba A., Sternberg A., van Dishoeck E. F., 2022, *ApJ*, 931, 28
- Ibáñez-Mejía J. C., Mac Low M.-M., Klessen R. S., Baczynski C., 2016, *ApJ*, 824, 41
- Joshi P. R., Walch S., Seifried D., Glover S. C. O., Clarke S. D., Weis M., 2019, *MNRAS*, 484, 1735
- Keating L. C. et al., 2020, *MNRAS*, 499, 837
- Kim C.-G., Ostriker E. C., 2018, *ApJ*, 853, 173
- Klessen R. S., Glover S. C. O., 2016, *Saas-Fee Adv. Course*, 43, 85
- Lada E. A., Blitz L., 1988, *ApJ*, 326, L69
- Lahén N., Naab T., Johansson P. H., Elmegreen B., Hu C.-Y., Walch S., Steinwandel U. P., Moster B. P., 2020, *ApJ*, 891, 2
- Larson R. B., 1981, *MNRAS*, 194, 809
- Lee M.-Y., Stanimirović S., Wolfire M. G., Shetty R., Glover S. C. O., Molina F. Z., Klessen R. S., 2014, *ApJ*, 784, 80
- Lee M.-Y., Stanimirović S., Murray C. E., Heiles C., Miller J., 2015, *ApJ*, 809, 56
- Lesaffre P., Pineau des Forêts G., Godard B., Guillard P., Boulanger F., Falgarone E., 2013, *A&A*, 550, A106
- Li M., Ostriker J. P., Cen R., Bryan G. L., Naab T., 2015, *ApJ*, 814, 4
- Li Q., Narayanan D., Davé R., Krumholz M. R., 2018, *ApJ*, 869, 73
- Lombardi M., Alves J., Lada C. J., 2006, *A&A*, 454, 781
- Luisi M. et al., 2021, *Sci. Adv.*, 7, eabe9511
- Madden S. C. et al., 2020, *A&A*, 643
- Melchior A. L., Viallefond F., Guélin M., Neining N., 2000, *MNRAS*, 312, L29
- Nelson R. P., Langer W. D., 1997, *ApJ*, 482, 796
- Nieten C., Neining N., Guélin M., Ungerechts H., Lucas R., Berkhuijsen E. M., Beck R., Wielebinski R., 2006, *A&A*, 453, 459
- Offner S. S. R., Bisbas T. G., Bell T. A., Viti S., 2014, *MNRAS*, 440, L81
- Ossenkopf V., 1997, *New Astron.*, 2, 365
- Ossenkopf V., Röllig M., Neufeld D. A., Pilleri P., Lis D. C., Fuente A., van der Tak F. F. S., Bergin E., 2013, *A&A*, 550, A57
- Pabst C. et al., 2019, *Nature*, 565, 618
- Padoan P., Pan L., Haugbølle T., Nordlund Å., 2016, *ApJ*, 822, 11
- Papadopoulos P. P., Thi W. F., Viti S., 2004, *MNRAS*, 351, 147
- Peters T. et al., 2017, *MNRAS*, 466, 3293
- Pineda J. E., Caselli P., Goodman A. A., 2008, *ApJ*, 679, 481
- Pineda J. L., Langer W. D., Velusamy T., Goldsmith P. F., 2013, *A&A*, 554, A103
- Pineda J. L., Langer W. D., Goldsmith P. F., 2014, *A&A*, 570, 121
- Rachford B. L. et al., 2009, *ApJS*, 180, 125
- Rathjen T.-E. et al., 2021, *MNRAS*, 504, 1039
- Rathjen T.-E., Naab T., Walch S., Seifried D., Girichidis P., Wünsch R., 2023, *MNRAS*, 522, 1843
- Ripple F., Heyer M. H., Gutermuth R., Snell R. L., Brunt C. M., 2013, *MNRAS*, 431, 1296
- Röllig M., Ossenkopf V., Jeyakumar S., Stutzki J., Sternberg A., 2006, *A&A*, 451, 917
- Salpeter E. E., 1955, *ApJ*, 121, 161
- Schöier F. L., van der Tak F. F. S., van Dishoeck E. F., Black J. H., 2005, *A&A*, 432, 369
- Scoville N. Z., Solomon P. M., 1975, *ApJ*, 199, L105
- Scoville N. Z., Yun M. S., Clemens D. P., Sanders D. B., Waller W. H., 1987, *ApJS*, 63, 821
- Seifried D., Walch S., 2016, *MNRAS*, 459, L11
- Seifried D. et al., 2017, *MNRAS*, 472, 4797
- Seifried D., Walch S., Reissl S., Ibáñez-Mejía J. C., 2019, *MNRAS*, 482, 2697
- Seifried D., Haid S., Walch S., Borchert E. M. A., Bisbas T. G., 2020a, *MNRAS*, 492, 1465
- Seifried D., Walch S., Weis M., Reissl S., Soler J. D., Klessen R. S., Joshi P. R., 2020b, *MNRAS*, 497, 4196
- Seifried D., Beuther H., Walch S., Syed J., Soler J. D., Girichidis P., Wünsch R., 2022, *MNRAS*, 512, 4765
- Sembach K. R., Howk J. C., Ryans R. S. I., Keenan F. P., 2000, *ApJ*, 528, 310
- Shetty R., Glover S. C., Dullemond C. P., Klessen R. S., 2011a, *MNRAS*, 412, 1686
- Shetty R., Glover S. C., Dullemond C. P., Ostriker E. C., Harris A. I., Klessen R. S., 2011b, *MNRAS*, 415, 3253

- Smith M. W. L. et al., 2012, *ApJ*, 756, 40  
 Smith R. J., Glover S. C. O., Clark P. C., Klessen R. S., Springel V., 2014a, *MNRAS*, 441, 1628  
 Smith R. J., Glover S. C. O., Klessen R. S., 2014c, *MNRAS*, 445, 2900  
 Smith R. J. et al., 2020, *MNRAS*, 492, 1594  
 Solomon P. M., Rivolo A. R., Barrett J., Yahil A., 1987, *ApJ*, 319, 730  
 Spitzer L., 1978, *Physical Processes in the Interstellar Medium*, Wiley-Interscience, New York  
 Stacey G. J., Geis N., Genzel R., Lugten J. B., Poglitsch A., Sternberg A., Townes C. H., 1991, *ApJ*, 373, 423  
 Strong A. W., Mattox J. R., 1996, *A&A*, 308, L21  
 Stutzki J., 2001, *Astrophys. Space Sci. Suppl.*, 277, 39  
 Sutherland R. S., Dopita M. A., 1993, *ApJS*, 88, 253 <http://dx.doi.org/10.1086/191823>  
 Tielens A. G. G. M., Hollenbach D., 1985, *ApJ*, 291, 722  
 Tiwari M., 2021, American Astronomical Society Meeting Abstracts. 53, p. 137.03  
 Valdivia V., Hennebelle P., Génin M., Lesaffre P., 2016, *A&A*, 587, A76  
 van Dishoeck E. F., Black J. H., 1988, *ApJ*, 334, 771  
 Velusamy T., Langer W. D., 2014, *A&A*, 572, A45  
 Waagan K., 2009, *J. Comput. Phys.*, 228, 8609  
 Walch S. et al., 2015, *MNRAS*, 454, 238  
 Walker K. M., Song L., Yang B. H., Groenenboom G. C., van der Avoird A., Naduvalath B., Forrey R. C., Stancil P. C., 2015, *American Astr. Soc.*, 811, 27  
 Wilson T. L., 1999, *Rep. Prog. Phys.*, 62, 143  
 Wilson R. W., Jefferts K. B., Penzias A. A., 1970, *ApJ*, 161, L43  
 Wünsch R., Walch S., Dinnbier F., Whitworth A., 2018, *MNRAS*, 475, 3393  
 Wünsch R., Walch S., Dinnbier F., Seifried D., Haid S., Klepitko A., Whitworth A. P., Palouš J., 2021, *MNRAS*, 505, 3730

## APPENDIX A: SUPPLEMENTARY FIGURES

In the following, we show some additional plots which help in clarifying several aspects of the paper. In Fig. A1 we show the same expanding bubbles as in Fig. 5, but now for the case with and without the post-processing for  $C^{2+}$  (see Section 3.2) to allow for a direct comparison. The importance of the post-processing in removing the [C II] intensity coming from the interior of the bubbles is evident, in particular for bubbles associated with older and hotter stars.

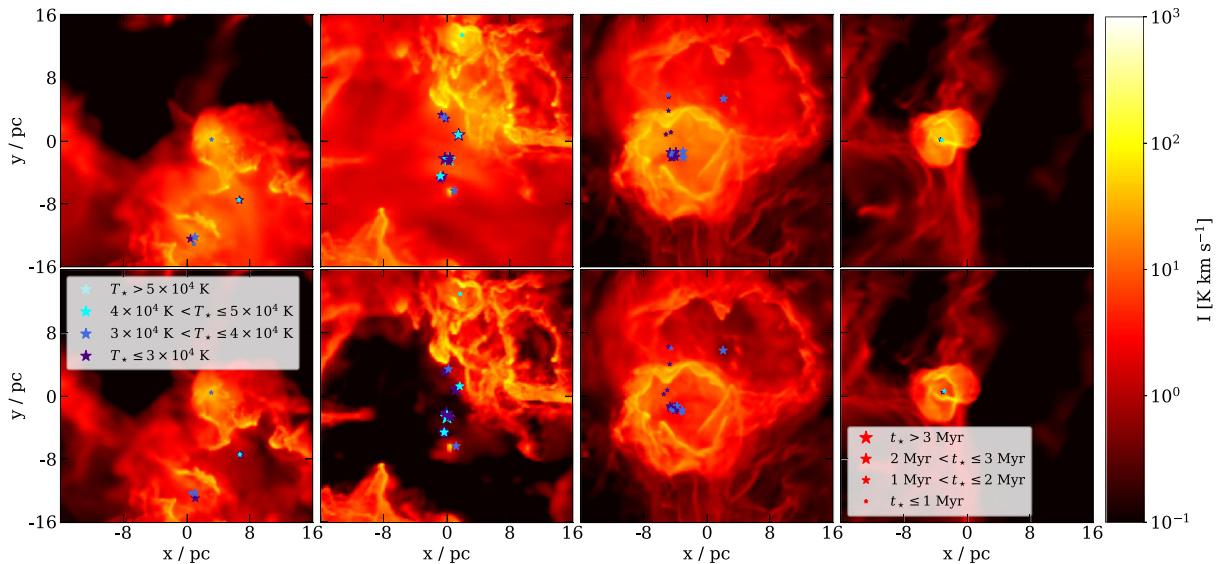


**Figure A1.** Examples of synthetic [C II] emission maps of expanding feedback bubbles, before (top row) and after the post-processing described in Section 3.2 to account for the conversion of  $C^+$  into  $C^{2+}$  (bottom row). The importance of the post-processing in reducing the [C II] intensity coming from the interior of the bubbles is evident, in particular for bubbles associated with older and hotter stars.

In Fig. A2 we show  $L_{12CO}/L_{[CII]}$  (left side) and  $L_{13CO}/L_{[CII]}$  (right side) as a function of the  $H_2$  mass, instead of the  $H_2$  mass fraction (see Fig. 8). The correspondence of the line ratio with the  $H_2$  mass is even weaker than with the  $H_2$  mass fraction. This is due to the fact that the mass is an extensive quantity, whereas line ratios and mass fractions are intensive quantities.

In Fig. A3 we show a scatter plot of  $I_{12CO}$  and  $I_{13CO}$  as a function of  $N_{H_2}$  for MC1-HD-noFB at  $t_{evol} = 4$  Myr, where each point represents a pixel of the image. The points are colour-coded by the excitation temperature (left column) or the optical depth (right column). We calculate the integrated  $^{12}CO$  optical thickness,  $\tau_{12CO}$ , using the common observational procedure (e.g. Arzoumanian et al. 2013)

$$\frac{I_{12CO}}{I_{13CO}} = \frac{1 - \exp(-\tau_{12CO})}{1 - \exp(-\tau_{13CO})} = \frac{1 - \exp(-\tau_{12CO})}{1 - \exp(-\tau_{12CO}/69)}, \quad (A1)$$

which can be solved for  $\tau_{12CO}$  using a Newton root finding algorithm. From this, the optical depth for  $^{13}CO$  is calculated as

$$\tau_{13CO} = \tau_{12CO}/69, \quad (A2)$$

assuming the default abundance ratio of 69 (Wilson 1999). The excitation temperature is calculated for each cell from the level population  $n_u$  and  $n_l$ , obtained with RADMC-3D, of the upper and lower states by using

$$\frac{n_u}{n_l} = \frac{g_u}{g_l} \exp\left(-\frac{h\nu}{k_B T_{ex}}\right). \quad (A3)$$

The quantity shown in the plot is then the mass-weighted  $T_{ex}$  along the LOS.

We note that at  $N_{H_2} \gtrsim 10^{21} \text{ cm}^{-2}$ , the  $^{12}CO$  line is largely optically thick, thus the intensity differences in that regime are mostly due to the different  $T_{ex}$ . The  $^{13}CO$  line becomes somewhat optically thick ( $\tau \gtrsim 1$ ) for  $N_{H_2} \gtrsim 10^{22} \text{ cm}^{-2}$ . This is reflected in the fact that both the relations if  $I_{12CO}$  and  $I_{13CO}$  with  $N_{H_2}$  flatten for  $N_{H_2} \gtrsim 10^{21} \text{ cm}^{-2}$ , but the slope change for  $^{13}CO$  is more gradual than for  $^{12}CO$ .

In Fig. A4 we show the line ratios using units of  $\text{erg s}^{-1}$  for the luminosity. This allows an easier comparison with some observational results e.g. by Röllig et al. (2006; see Section 5.1).

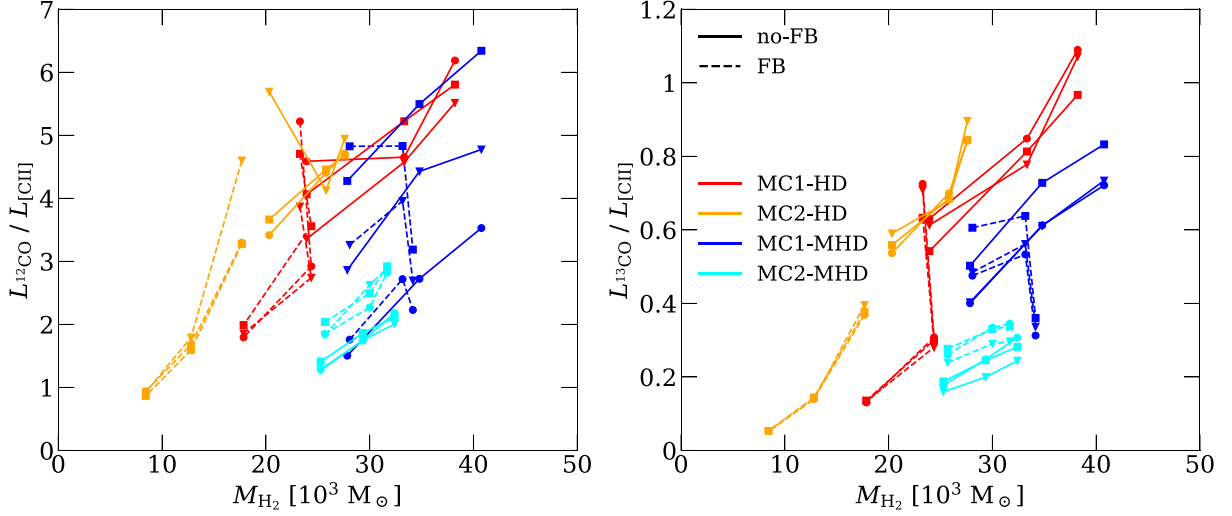


**Figure A2.**  $L_{12\text{CO}}/L_{[\text{CII}]}$  (left-hand panel) and  $L_{13\text{CO}}/L_{[\text{CII}]}$  (right-hand panel) as a function of the  $\text{H}_2$  mass as opposed to Fig. 8 where it is plotted against  $M_{\text{H}_2}/M_{\text{H,tot}}$ . As the luminosity ratio is an intensive property of the clouds, while the  $\text{H}_2$  mass is extensive, the relation shows an even larger scatter than the one against the  $\text{H}_2$  mass fraction (see Fig. 8).

In Fig. A5 we show the mean of  $I_{[\text{CII}]}$  as a function of  $2 \times N_{\text{H}_2}/N_{\text{H}}$ , *pixel-by-pixel*, for all our clouds and snapshots and overplot the observational data from Hall et al. (2020). We find that the observational data are shifted slightly towards higher values of  $2 \times N_{\text{H}_2}/N_{\text{H}}$ . Beside intrinsic observational uncertainties, one possible reason for this shift could be due to the fact that Hall et al. (2020) use  $N_{\text{H}}$ -data which are opacity-corrected by Lee et al. (2015), also by means of H I absorption measurements. However, as discussed in Seifried et al. (2022), the calculation of  $N_{\text{H}}$  by means of absorption measurements usually leads to an underestimation of  $N_{\text{H}}$  by up to a factor of a few. This would shift the ratio of  $2 \times N_{\text{H}_2}/N_{\text{H}}$  towards higher values i.e. towards the right as indeed observed in Fig. A5. An additional uncertainty in this comparison arrives

from the differences in the environmental conditions. As stated before, the Perseus cloud has a lower ISRF which also affects the  $2 \times N_{\text{H}_2}/N_{\text{H}}$  ratio. All in all, given these uncertainties, we consider the match between our and the observational data as reasonable.

In Fig. A6 we show a 2D-PDF of the gas temperature and the excitation temperature for MC1-HD-noFB at  $t_{\text{evol}} = 2$  Myr. The upper plot refers to the non-equilibrium (i.e.  $t_{\text{chem}} = 0$ ), and the bottom plot refer to the equilibrium state ( $t_{\text{chem}} = 50$  Myr) as discussed in Section 5.2. Due to the changes in the collisional partners (see Fig. 13), the excitation temperature is lower at equilibrium, which explains why the [C II] luminosity decreases when evolving the chemistry to equilibrium.

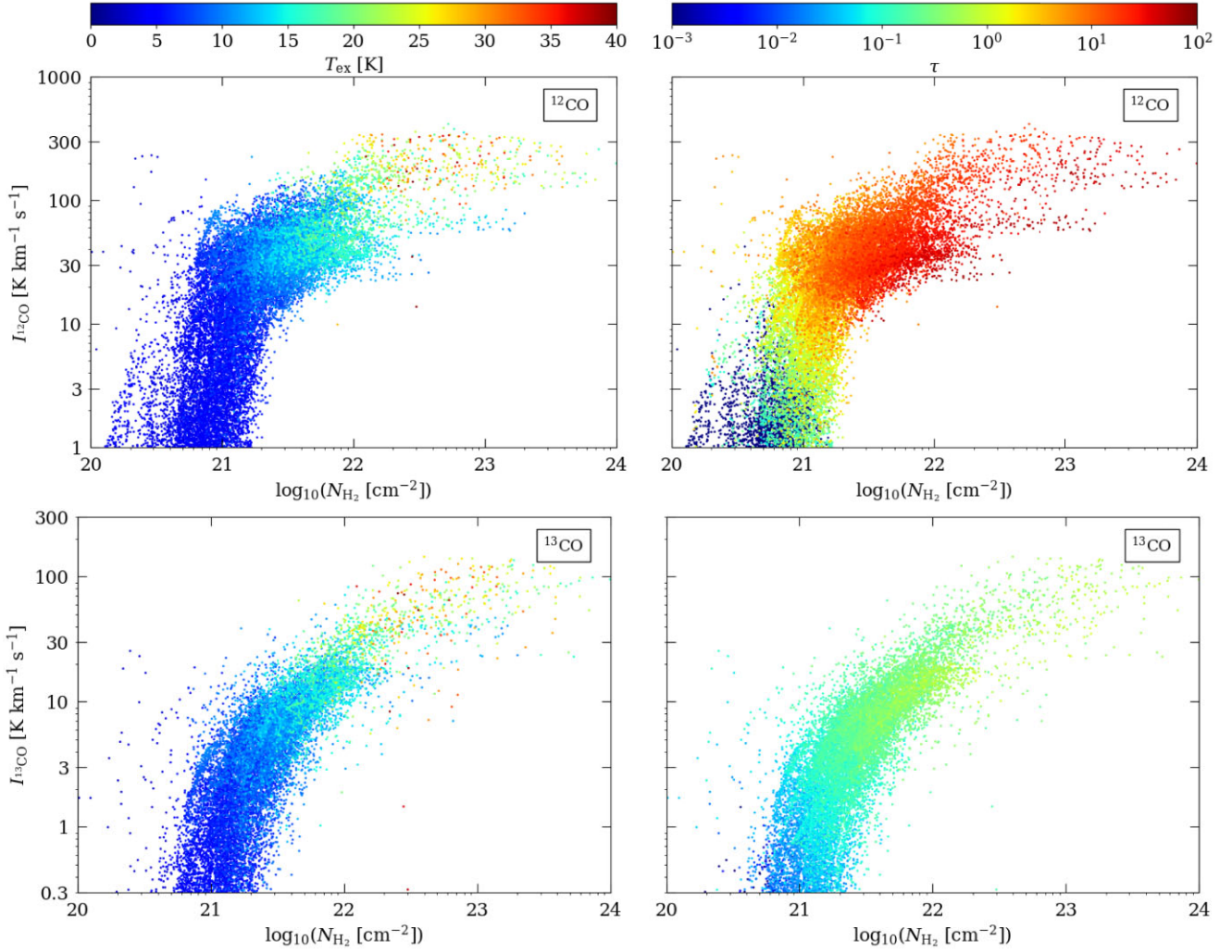


**Figure A3.**  $I_{^{12}\text{CO}}$  (top row) and  $I_{^{13}\text{CO}}$  (bottom row) as a function of the  $\text{H}_2$  column density for MC1-HD-noFB,  $t_{\text{evol}} = 4$  Myr, seen along the  $z$ -axis. Every point represents a pixel of the image. Colours represent the excitation temperature ( $T_{\text{ex}}$ , left) and the integrated optical depth  $\tau$ . The  $^{12}\text{CO}$  line is optically thick for  $N_{\text{H}_2} \gtrsim 10^{21} \text{ cm}^{-2}$ , and the still moderate increase of  $I_{^{12}\text{CO}}$  above this values is due to the increase in  $T_{\text{ex}}$ . The  $^{13}\text{CO}$  line only has  $\tau \gtrsim 1$  for  $N_{\text{H}_2} \gtrsim 10^{22} \text{ cm}^{-2}$ , and therefore optical depth has a minor impact in shaping the  $I$ - $N$  relation.

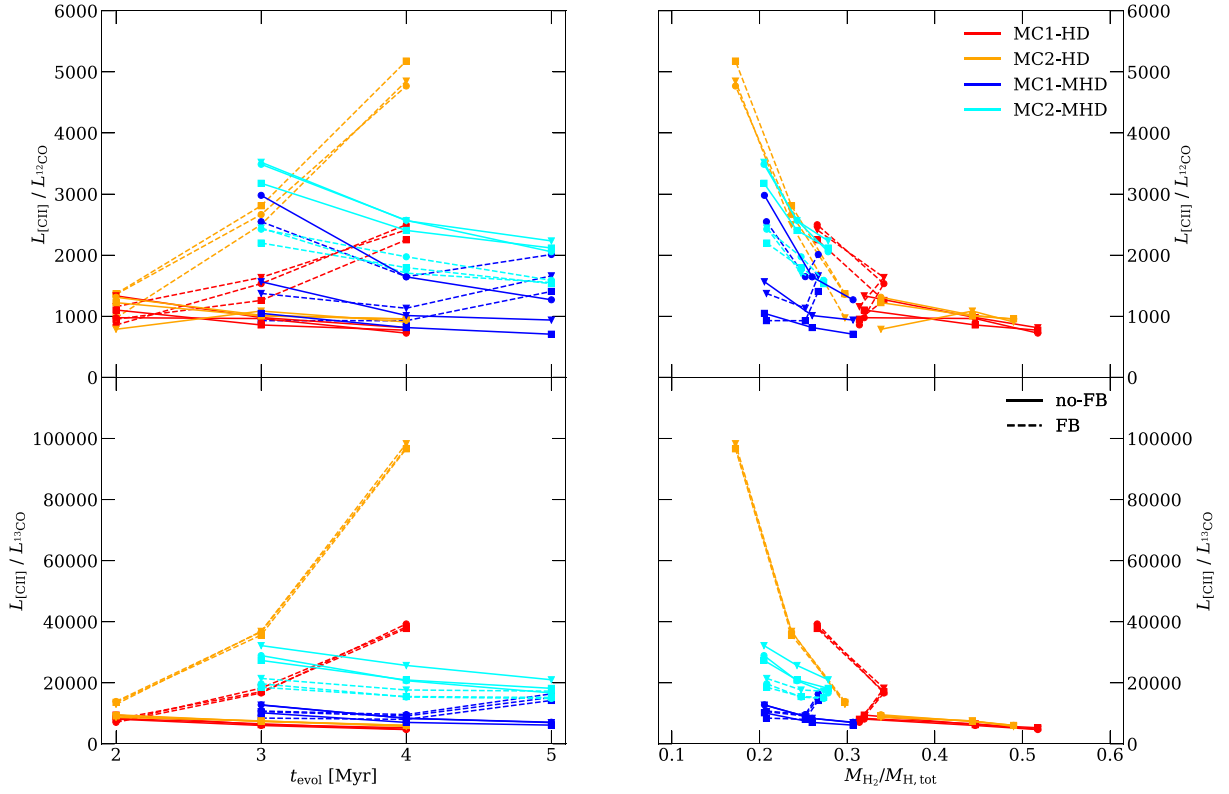


**Figure A4.**  $L_{\text{CII}}/L_{12\text{CO}}$  (top row) and  $L_{\text{CII}}/L_{13\text{CO}}$  (bottom row) as a function of  $t_{\text{evol}}$  (left column) and  $M_{\text{H}_2}/M_{\text{H,tot}}$  (right column). Luminosities are expressed in  $\text{erg s}^{-1}$  as opposed to the usage of  $\text{K km s}^{-1}$  in the main body of the paper.

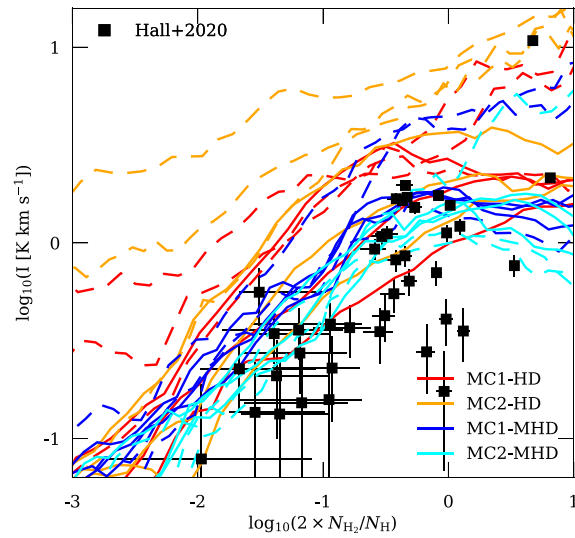


**Figure A5.** Same as Fig. 10, but as a function of  $2 \times N_{\text{H}_2}/N_{\text{H}}$  and only for  $I_{\text{CII}}$ . The black squares represent the observational data from Hall et al. (2020). The observational are shifted slightly to the right, possibly due to an underestimation of  $N_{\text{H}}$ .

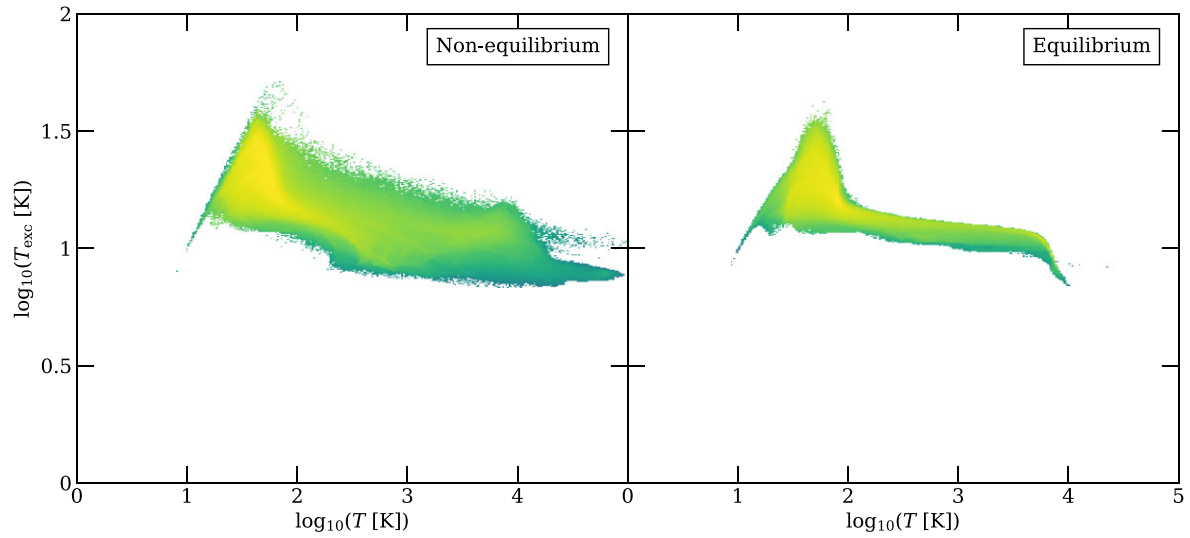


**Figure A6.** 2D-PDF of excitation temperature  $T_{\text{ex}}$  as a function of the gas temperature. The left-hand side plot represents MC1-HD-noFB at  $t_{\text{evol}} = 2$  Myr with the chemistry evolved *on-the-fly*; the right-hand side plot represents the same snapshot at steady state i.e. at  $t_{\text{chem}} = 50$  Myr.

This paper has been typeset from a  $\text{\TeX}/\text{\LaTeX}$  file prepared by the author.